A Dislocation Model of the 1994 Northridge, California, Earthquake Determined From Strong Ground Motions

By

David J. Wald and Thomas H. Heaton

U.S. Geological Survey
525 S. Wilson Ave
Pasadena, California, 91106

Open-File Report 94-278

OUTLINE

ABSTRACT

A preliminary rupture model of the 1994 Northridge, California earthquake, determined from strong motion waveform inversion and analysis, is presented. The fault rupture plane chosen is based on the distributions of aftershocks and teleseismic surface-wave and body-wave point-source solutions. The fault strikes 122°, dips 42°, and has a slip vector of 109°. The average slip is about 1.2 meters over the rupture area and the peak slip reaches nearly 4 meters. Our estimate of the seismic moment is $1.2 \pm 0.2 \times 10^{26}$ dyne-cm. The area of rupture is small relative to the aftershock dimensions and is approximately 14 km along strike (west-northwest from the hypocenter) and nearly 20 km in the updip direction. There is little indication of slip shallower than about 7 km.

The up-dip, near-source strong-motion velocity waveforms show two distinct, large S-wave arrivals 2-3 sec apart (as do the teleseismic P waves), indicating separate source subevents. An along strike (west-northwest) subevent separation of about 8 km is most consistent with the observation that the two main arrivals are separated more in time to the south and southeast (about 4.5 sec at Stone Canyon Reservoir and Sherman Oaks, for example), than at northern azimuths. The interpretation of secondary arrivals observed at more distant stations to the south and southeast (e.g., Santa Monica) is more tenuous, since several of the aftershocks recorded there indicate later arrivals as well. However, a secondary source contribution is expected based on our model of the closer stations.

After placing these constraints on the general nature of the rupture, we predict the characteristics of the long-period (1-10 sec) ground velocities over a grid of stations covering the near-source region. This exercise provides a basis for separating the effects of source radiation (dominated by radiation pattern and directivity) from the complex waveform modifications due to wave-propagation and site response.

INTRODUCTION

The January 17, 1994 Northridge (M_w = 6.7) earthquake produced the largest ground motions ever recorded in an urban environment and caused the greatest damage in the United States since the great 1906 San Francisco earthquake (U.S.G.S and S.C.E.C., 1994). Peak acceleration and velocity values were among the largest ever recorded in any earthquake, and the large number of strong-motion recordings is unprecedented. Additionally, extensive portable instrument deployments for recording aftershocks will provide calibration data for understanding the mainshock strong motions. The extent of the damage and the abundance of recorded ground motions necessitate a systematic analysis and understanding of the source and nature of the ground motions and resulting damage patterns.

This report is intended to provide a preliminary, working rupture model for the Northridge earthquake for use in ongoing studies of the source, wave propagation and site effects as well as engineering and damage analysis. For this reason, we have tabulated the important rupture properties (Table 4) and provided the spatial and temporal details of the the slip model (Table 5).

In this analysis, we first examine the variations and systematics of the near-source (distances within 1-2 source depths) recorded ground motions. We map the spatial distribution of the ground motions at several different bandpassed frequency ranges, allowing the local waveform and amplitude variations to be visualized. By gradually shifting the frequency bandpass towards longer periods, the effects of source and propagation can be differentiated. We then invert the bandpassed (1-10 sec) velocity ground motions to determine the spatial and temporal distribution of slip on the fault rupture plane. The resulting dislocation model is tested against the teleseismic bodywave observations and is also used to predict the source contributions to the general characteristics of the long-period ground motions over the entire epicentral region. Finally, we make some general comparisons with other recent California earthquakes as well as the 1971 San Fernando earthquake.

The results of this study are preliminary in nature; several sources of data were still in the processing stage or were not made available at the time of this publication. These sources include several near-source, strong-motion accelerograms, an immense geodetic data set made

up of both line-leveling and horizontal and vertical displacements of GPS survey stations, and much of the aftershock data from portable station deployments at strong-motion stations which recorded the mainshock. We expect to update and improve our working model based on the updated data sets; however, we feel the results presented here are robust with respect to the general source dislocation features.

FAULT RUPTURE MODEL

Fault Parameterization

In order to model slip during the Northridge earthquake, we chose a single fault plane that is consistent with a broad range of observations. The fault plane dips 42° and passes directly through the relatively simple, planar aftershock distribution (Figure 1). We use a strike of 122°, compromising between the different solutions found from modeling teleseismic surface-waves (Harvard CMT) and body-waves (Thio and Kanamori, 1994) which indicate strikes near 130°, and the first-motion mechanism (U.S.G.S. and S.C.E.C., 1994) which requires a strike between 100° – 110°. Further, vertical cross-sections of the eastern half of the aftershock distribution present the simplest planar structure when projected perpendicular to a 120° strike. The rake vector was fixed at 109° based on the above solutions. However, as discussed later, we also allowed the rake vector to vary to test this assumption.

The overall fault dimensions were initially determined based on the teleseismic time function (Thio and Kanamori, 1994) which suggested a total rupture duration of about 7 sec. The fault length is 18 km and the down-dip width is 20.9 km. These dimensions proved suitable due to the compact nature of the Northridge rupture. We discretized the fault plane into a total of 196 subfaults in order to represent variable slip along the fault. The fault parameterization and modeling procedure we employ is described by Hartzell and Heaton (1983).

Synthetic Green's Functions

The subfault motions are obtained by summing the responses of nine point sources equally distributed over the subfault. Each point source is then lagged appropriately in time to include the travel time difference due to the varying source-to-station positions and to simulate

the propagation of the rupture front across each subfault. Thus, all subfaults separately include the correct effects of directivity.

Point source response for the teleseismic *P* or *SH* body-wave synthetic seismograms are computed using the generalized ray method (Langston and Helmberger, 1975). We include the responses of all rays up to two internal reflections in a layered velocity model (Figure 2), including free surface and internal phase conversions. A Q operator is applied with the attenuation time constant t^* equal to 1.0 and 4.0 sec for *P* and *SH* waves, respectively.

The point source responses for the strong-motion synthetics are computed for the same layered velocity model (Figure 2) with a discrete-wavenumber, finite-element (DWFE) scheme (Olsen *et al.*, 1984) for frequencies up to 3.0 Hz. In practice, we calculate a master set of synthetics for 1 km increments in depth from 5.0 to 22.0 km and for ranges between 0 and 60 km, to allow for the closest and furthest possible subfault-station combinations. Then for each point source-station pair, the required response is derived by a linear interpolation of the closest Green's functions available in the master set. The linear interpolation of adjacent Green's functions is performed by aligning the waveforms according to their shear-wave travel times. The final, subfault synthetic is obtained by the summation of nine point source responses, appropriately lagged in time for the rupture delay.

The source-region velocity model used to compute the strong-motion Green's functions shown in Figure 2 is modified from Langston (1978, Model C). We have added a thin (0.5 km), slower layer to Langston's model to better approximate elastic properties just beneath the strong-motion stations. Minor variations on this model have been used extensively (e.g., Dreger and Helmberger, 1990) for modeling many regional waveforms in Southern California.

Source Time Function And Rupture Velocity

The dislocation time history for each subfault is represented by the integral of an isosceles triangle with a duration of 0.6 sec. Each subfault is also allowed to slip in any of three identical 0.6 sec time windows following the passage of the rupture front, with each window separated by 0.3 sec, so that they overlap in time and thus can provide a smooth overall slip history, if necessary, lasting up to 1.2 sec.

With multiple time windows we can approximate both variable, complex, or long duration local slip histories and rupture velocity perturbations from the assumed uniform velocity as is

discussed by Wald and Heaton (1994). However, we find little indication of such complexities for the Northridge rupture, and our final model allows only one episode of slip following the passage of the rupture front.

The rupture velocity is assumed to be a constant 2.8 km/sec, or about 70% of the shear wave velocity in the main part of the source region (Figure 2). We iterated through a range of values from 2.7 to 3.3 km/sec but found a rupture velocity of 2.8 km/sec provided the best fit to the data.

Rupture Initiation

Evidence from the strong-motion data indicates that the initial rupture was rather subdued, reminiscent of delayed initial growth of the Loma Prieta (Wald *et al.*, 1991) and Landers earthquakes (Abercrombie and Mori, 1994). As shown in Figure 3, trigger times, when available, indicate that the triggering P wave arrived at least 0.5 seconds later than expected given the predicted travel time from the hypocentral parameters. Further analysis by Ellsworth and Beroza (1994) suggests that a small nucleation phase of the rupture was followed by a secondary, larger rupture episode beginning near the hypocenter approximately 0.5 seconds later, consistent with the delayed strong-motion trigger times.

We used the origin time of 12:30:55.2 GMT and a hypocentral depth of 18.5 km determined by relocating SCSN network phase data (E. Hauksson, written communication, 1994). Based on the above observations, we initiate the first time window 0.5 sec after the hypocentral time. We thus chose to ignore the foreshock or initial rupture and began modeling at the time of the first significant rupture episode. We assumed that the main (secondary) rupture began at or near the network hypocenter location and then allowed the rupture to propagate radially outward from that location.

Inversion Method

A constrained, damped, linear, least-squares inversion procedure is used to obtain the subfault dislocation values which give the best fit to the strong-motion velocity waveforms. The inversion is constrained by requiring that the slip is everywhere positive, and it is damped by minimizing the difference in dislocation values between adjacent subfaults. These constraints have been previously discussed by Hartzell and Heaton (1983). Solving for the amplitude

of slip on each subfault given the strong-motion observations and subfault synthetic seismograms, is posed as an overdetermined system of linear equations,

$$\mathbf{Ax} \cong \mathbf{b}, \tag{1}$$

where $\mathbf{A}$ is the matrix of subfault synthetics, x is the solution vector consisting of subfault slip weights, and b is the data vector. The damping is included by appending a number of rows to the equations:

$$\begin{pmatrix} \mathbf{C_d^{-1}A} \\ \lambda_1 \mathbf{S} \end{pmatrix} \mathbf{x} \cong \begin{pmatrix} \mathbf{C_d^{-1}b} \\ \mathbf{0} \end{pmatrix}. \tag{2}$$

Here $\mathbf{C_d^{-1}}$ is an *a priori* data covariance matrix which normalizes and weights the data and $\mathbf{S}$ is a matrix of smoothing constraints which minimize the slip difference between adjacent subfaults ($x_i - x_{i+1} = 0$), both along strike and downdip. Linear weight λ_1 controls the tradeoff between satisfying the smoothing constraints and fitting the data.

STRONG MOTION DATA AND PRELIMINARY ANALYSIS

In our analysis we use strong-motion accelerograms from the California Division of Mines and Geology (Shakal *et al.* 1994), the U.S. Geological Survey (Porcella *et al.*, 1994), the Los Angeles Department of Power and Water, and Southern California Edison. Table 1 lists the station abbreviations and locations as well as other site specifications, and the distribution of stations is displayed in Figure 4. Where two or more stations were located in close proximity to each other, a representative location was chosen for our analysis.

The stations presented here are those available to us in digital or digitized form at the time of this study. In time, digitized data from many other stations should be available; however, we do not expect substantial improvement of the near-source station coverage over what is shown in Figure 4. As indicated in Table 1, the data consist of SMA-1 analogue recordings digitized by the C.D.M.G., SMA-1 recordings scanned and digitized by the authors, and digital force-balance accelerometer (FBA) records.

The variability of the ground motions in the Northridge earthquake is examined in map view in Figures 5a through 5f. Each waveform trace is associated with a nearby station

location (shown with open symbols) and both waveform amplitude and time scales are displayed to the right. In each figure, the waveform amplitudes are plotted with a common scale for direct comparison. The dashed rectangle depicts the map projection of the inferred fault plane. Lightly shaded areas indicate Quaternary alluvium, which delineates the basin and valley regions, including the Los Angeles Basin, the San Gabriel Valley, and the San Fernando Valley which is directly above and southeast of the inferred rupture plane.

Figures 5a and 5b show the unfiltered acceleration recordings, Figures 5c and 5d show the high-pass filtered velocity waveforms, and Figures 5c and 5f show the bandpassed (1.0-10 sec) velocity data. Since the integration from acceleration to velocity enhances lower frequencies, this sequence of figures allows the spatial waveform and amplitude variations to be visualized as the frequency bandpass is progressively shifted towards longer periods. Effectively, this allows us to separate some of the effects of wave propagation and site response, which are most profound in the unfiltered accelerations (Figures 5a and 5b), from the more obvious contributions to the ground motions from the source rupture directivity and radiation pattern, which dominate the longer-period velocity waveforms (Figures 5c and 5d).

Ideally, we would like to learn to separate the ground motion contributions that can be attributed to the earthquake source from those that are due to wave propagation and site response. While the nature of the source can vary greatly, much of the path and site effects are deterministic features of the specific location and are, hence, ultimately predictable. This approach, of course, will not isolate longer-period wave propagation phenomena often found to dominate strong-motion velocity and displacement data such as basin reverberations and body-to-surface wave conversions (e.g., Liu and Heaton, 1984; Vidale and Helmberger, 1988; and Frankel, 1994).

The variability of ground motions observed can be ascribed to a number of factors in addition to source distance. The ground velocities north of the epicenter are dominated by simple, large amplitude pulses indicative of northward, updip source directivity. In the region 10-25 km north-northeast of the epicenter, where we would expect the combined effects of radiation pattern and directivity to be maximized for this fault geometry, the recorded ground velocities are among the largest ever recorded. In fact, the recorded peak horizontal

ground velocity at the free-field site near the county hospital in Sylmar (stations SYL, 15 km north-northeast of the epicenter) was about 130 cm/sec; the peak velocity was over 170 cm/sec at the Los Department of Water and Power Renaldi Receiving station (RRS) several km to the south. The Renaldi ground velocity is the largest recorded to date from *any* earthquake. These large velocity recordings require impressive particle velocities at the rupture surface, which being deep, is at least 7 km from any of these recordings.

These large, updip recorded ground velocities are significant, since at least for many larger structures, peak ground velocity is a better measure of damage potential than is peak ground acceleration (EERI, 1994). It is important to note that much of the updip region where directivity effects dominate, is not as densely populated as regions to the south, which is fortunate considering the nature of the recordings. There were, though, several notable freeway failures in this region, including the two collapses at the I5/SR14 interchange and at the I5 Gavin Canyon undercrossing.

The effect of directivity is less obvious in the peak acceleration data (Figures 5a and 5b). For example, several of the larger peak accelerations were located south of the epicenter where the large amplitudes were likely dominated by propagation and site effects rather than source radiation alone. As in other earthquakes, soft soils and topographic features may have produced higher ground motions locally. When the aftershock data have been collected and more fully analyzed, more details pertaining to the site conditions and effects will be understood.

STRONG MOTION INVERSION

When the trigger time was available, synthetic and observed waveforms were aligned in absolute time and only minor corrections (given in Table 2) were made for static station delays or timing errors. For all other stations, the synthetic S waves from the subfault containing the hypocenter were aligned with the initial S wave in the data. Since the synthetic S wave has a similar waveshape to the data, this approach allows us to make a direct comparison and alignment with the observed S waveform.

All station observations are scaled to a unit amplitude in the inversion in order to insure equal importance of smaller amplitude stations and to down-weight possible site effects.

Careful examination of the ground-motion recordings shows that, at adjacent stations, more variability was found in the vertical components, suggesting more contamination from site and path effects in the vertical data. For this reason, the vertical components were down-weighted by a factor of two with respect to the horizontal components at each station. We do not show the vertical components at stations SSU and MNG since their vertical traces were difficult to digitize; they may be added later when careful digitization is made.

With the exception of CAS and VSQZ (Figure 4), all the stations used in the inversion have horizontal distances of less 26 km from the center of the fault. We avoided more distant stations and those within the Los Angeles Basin since many of the aftershock recordings at these locations indicate waveform modifications caused by wave propagation through complex structures. We further focused on those stations almost or directly above the rupture surface (ENR, JFP, NHL, PDM, PKC, RRS, SHR, SSU, SVA, SYL, VNY), which have direct S wave travel paths that are adequately modeled with a simple layered velocity model, by weighting them a factor of 2 higher than more distant stations.

The accelerograms were bandpass-filtered between 0.1 and 1.0 Hz with a zero-phase, third-order Butterworth filter and were then integrated to obtain ground velocity. This bandpass was chosen to avoid long-period integration noise and to avoid inadequacies of the theoretical Green's functions at higher frequencies. Our inability to adequately estimate strong-motion Green's functions at frequencies higher that 1.0 Hz is limited in part by our lack of knowledge of the crustal velocity structure, but is also limited by the lack of absolute time at most strong-motion sites. The use of velocity rather than acceleration further emphasizes longer period characteristics of the strong motions. With better analyses of the local velocity structure, both through travel-time tomography and aftershock waveform studies, this high-frequency limit may be extended. But again, without absolute time at most of the mainshock stations, the ultimate resolution for this earthquake may be limited.

We modeled between 15 to 20 sec of the strong-motion records (Fig. 6), depending on the duration at individual stations. We do not rotate the stations to fault normal and parallel, since for stations above the fault, rotation is ambiguous. However, in order to facilitate waveform comparisons, all horizontal components are rotated to north and east, if not so recorded.

RESULTS

The strong motion inversion using a single 0.6 sec time window results in the slip distribution shown in Figure 7. The top portion of the figure shows the contoured slip (0.5 meter contour interval) with concentric circles depicting the advance of the rupture front at 1 sec intervals. The lower portion of the figure depicts the rake direction and the relative amplitude of slip on each subfault.

In order to test for more complexity in the rupture process, we also ran inversions using three 0.6 sec time windows, allowing the windows to overlap in time by 0.3 sec. A very similar slip distribution was obtained (Figure 8), suggesting that a simple, short slip duration over the entire rupture surface is adequate to model the gross features of the strong-motion data. Further examination of the make-up of the three time windows (Figure 9) indicates that most of the slip occurred in less than 1 sec over most of the fault. Figure 10 allows the visualization of the rupture by showing the slipping portion of the fault at one sec intervals. The entire rupture is over in approximately 7 sec.

A comparison of the strong-motion observations (top trace) and synthetics (bottom trace) for the single-time window dislocation model (Figure 7) is given in Figure 6. Observed amplitudes are given to the right of each trace in cm/sec and all are normalized to their peak value. The overall waveforms, both in amplitude and phase, are well matched by the synthetic ground motions at most stations.

Our overall slip pattern is in notable agreement with most of the features found in the slip pattern determined by Dreger (1994) using an empirical Green's function deconvolution of regional waveform data, and both models require a substantial amount of slip north-northwest of and at a comparable depth to the hypocenter. The slip variations in our model are also consistent with the subevents found by Thio and Kanamori (1994) from their waveform inversion of teleseismic bodywaves. Their solution shows the first subevent at 19 km, followed 2 sec later by a larger subevent at about 17 km, and finally, a third, smaller subevent, yet 2 sec later, at about 13 km. Presumably their second subevent at 17 km corresponds to our asperities at 15 and 19 km combined, and their third subevent relates to the shallower portion of our rupture model.

We also tested for slip rake variations by allowing the rake vector to vary as a function of position on the fault. The rake was constrained to vary between 60° and 150°. The resulting rake vectors were consistent with the assumed rake value, and there was not enough improvement to the waveform fits to justify the added freedom and complexity in the inversion.

DISCUSSION

The general pattern of the strong motion duration and waveform complexity can be partially explained by the relative position of individual stations with respect to the two lobes of concentrated slip shown in Figure 7. We considered the contributions to the ground motion from two regions of slip in the rupture model. The first region (S1) consists of the asperity between 9 and 16 km along strike and from 10 to 20 km in depth. The second region (S2) is the arcuate zone of slip from 3 to 9 km along strike, ranging from 7 to 20 km in depth. In Figures 11a and 11b, for selected strong motion stations, we display the observed (top trace) and the synthetic (second trace) records along with the separate contributions to the synthetic records from the source model regions S1 (third trace) and S2 (bottom trace). The relative amplitudes of the S1 and S2 *S* wave arrivals are dominated by the closest asperity to the station and show less of a contribution from the further slip concentration. At VNY, which is directly above source region S1, the S1 contribution dominates. The S2 arrival becomes more important at SSU, which is closer to S2. This is attributable to both the additional distance from the further lobe of concentrated slip and the favorable source radiation pattern for stations above the rupture surface.

Our dislocation model best predicts the waveform features at the near-source stations (JFP, PDM, RRS, SSU, SVA, SYL, and VNY). At these sites, the waveforms are dominated by up-going, direct *S* waves with short horizontal-to-vertical travel paths. At the more distance stations (CAS, MOR, MNG, and TPG) the later portions of the waveforms are not fit as well with the given source model. This is likely due to propagational complexities not included in our simple 1-D Green's functions rather than missing later source radiation, which would also be seen on the near-source recordings.

A current shortcoming of our initial model is the poor fit to the second arrival on the north component at stations SSC, SCR, and SHR. We hope to address this with careful aftershock

analyses for these sites. Extending our source analysis to higher frequencies and simulating the additional complexities at more distant stations will also require careful analysis of aftershocks recorded at mainshock strong-motion sites. Ultimately, the use of improved theoretical Green's functions incorporating 2- and 3-D earth structure, or employing empirical Green's functions for modeling complex path effects will be required.

It is often difficult to estimate stress drop for earthquakes since one must normally make assumptions concerning the relationship of the known rupture duration with the unknown rupture area. Our finite fault modeling approach allows us the advantage of determining both the amount of slip and the area over which it occurred. Even so, the stress drop calculation is only approximate, since it is difficult to determine where the slip goes to zero (and hence the rupture area). For our slip model, the stress drop expression of *Eshelby* [1957] for a circular fault is appropriate, $\Delta\sigma = (7\pi\mu\overline{u})/(16a)$, where μ is the rigidity, $\overline{u}$ is the average dislocation, and a is the radius. Using μ = 3.6 x 10^{11} dyne cm^{-2}, $\overline{u}$ = 121 cm, and a = 8.7 km, we obtain a stress drop of 70 bars.

There are serious ramifications to our observation that damaging ground motion radiation can be attributed to such a compact fault region. It is often considered that fault segmentation limits the maximum size of earthquakes that can occur along a given fault zone. The relatively large localized slip in the Northridge earthquake suggests that thrust faults of even limited dimensions are capable of producing destructive ground motions. This is substantiated by the high stress drops and substantial ground motions from the 1991 Sierra Madre (M_L=5.8) and the 1987 Whittier Narrows (M_L=5.9) earthquakes. Recall the area that actually slipped is substantially smaller than the region which experienced aftershocks.

We can compare the rupture area and amount of slip for the Northridge earthquake with other previously studied earthquakes (Figure 12). With increasing magnitude, earthquakes normally have larger rupture areas, peak slips, and average slip values. The 1991 Sierra Madre earthquake (M_w = 5.6) slipped less than one meter over just a few square km (Wald, 1992). In contrast, the 1992 Landers earthquake (M_w = 7.2) slipped up to 7 meters, and had a fault length of nearly 70 km (Wald and Heaton, 1994). The model of slip determined for the Northridge earthquake (M_w = 6.7), when compared to the slip from the larger 1989, M_w = 6.9, Loma Prieta earthquake (Wald *et al.*, 1991), indicates a considerably smaller

slip area and yet a comparable maximum slip. This large slip over a small area during the Northridge earthquake was one reason the ground motions were larger than for other similar magnitude earthquakes.

We can also make a direct comparison of the 1971 San Fernando and 1994 Northridge earthquakes by examining their rupture areas in map view and in cross-section (Figure 13). The San Fernando slip model is from Heaton (1982). The contoured slip (Figure 13, bottom) represents the summation of the slip from the two fault planes (Figure 13, Top) that ruptured during the 1971 event based on the Heaton model. Note that the areas and slip values are comparable for the 1971 and 1994 events, as are the moment magnitudes (M_w = 6.7). As has been observed with other earthquakes, there is a strong tendency of aftershocks to concentrate at the edges of high slip concentrations, indicating a redistribution of stresses in these areas (e.g., Mendoza and Hartzell, 1988)

Forward Prediction of Ground Motions

Now that we have a working source rupture model of the Northridge earthquake, one that predicts the main features of the recorded ground velocities, we can estimate what the motions were like at locations other than those which actually recorded data. This allows us to look at systematic variations in the ground motions which can be attributed solely to the source radiation (dominated by radiation pattern and directivity), and provides a basis for separating these effects on the recorded ground motions from the complex waveform modifications due to wave propagation and site response.

Using the dislocation model described above for the source (Fig. 7), we computed synthetic ground velocities for a grid of stations 58 km long in the east-west direction and 51 km in the north-south direction (circles in Fig. 14). The station spacing is approximately 5 km. In all, ground motions were computed at 144 locations in addition to the 26 stations explicitly included in the waveform inversion. Since the inverted ground motions were band-limited (1 to 10 sec), we only predict ground motions within this frequency range.

The peak value of ground velocity was determined at each grid station and these values were then contoured over the region. The contours of peak velocity are displayed in Figure 14 with a contour interval of 10 cm/sec. Again, peak velocity amplitudes are only given

within the bandwidth of the inversion modeling (1 to 10 sec). Since filtering the observed velocity data in this bandpass significantly reduces the peak values, we expect that the peak values shown in Figure 14 are similarly reduced. The spatial distribution and variation of the waveforms predicted in the forward model is depicted in Figures 15a and 15b for the north and east components of ground velocity, respectively.

The combination of radiation pattern and updip directivity conspire to produce the largest ground velocities directly updip from the fault (to the north-northeast) as observed, as well as to the north-northwest, where there are fewer data. Abrupt change in amplitudes are apparent as SV and SH radiation patterns become nodal.

The simple amplitude decay with distance, and the lack of waveform complexity at greater distances in the forward prediction points clearly to the inadequacy of a simple 1-D layered velocity model used to compute the strong-motion Green's functions. For this reason, we consider the features at stations near the boundaries of the grid to be less accurate than those in the center of the grid.

Forward Prediction of Teleseismic Bodywaves

We do not expect that the teleseismic data will greatly improve the resolution of the slip on the fault plane relative to the strong-motion inversion alone. The small horizontal extent of the source (10 km) and short rupture duration (about 7 sec) limit the resolving power of the teleseismic data. It is the azimuthal variations in waveforms due to rupture directivity that usually provide the best information for source imaging. However, rupture directivity plays an important role only when the rupture front progresses at a velocity comparable to the phase of interest (Heaton, 1982, Appendix). Unless the horizontal extent of the rupture is large, teleseismic waveforms are more sensitive to up- and downdip rupture, since the vertical-phase velocity is comparable to the rupture velocity, and the horizontal-phase velocity is much higher than the rupture velocity. Nevertheless, the teleseismic data do provide an independent check on the strong-motion model. Naturally, we can place more confidence in our strong-motion source model if it fits the teleseismic data as well, even though the teleseismic data was not used explicitly in the waveform inversion.

The teleseismic station locations for the broadband data used in this study are listed in

Table 3 and their azimuthal distribution with respect to the *P* and *SH* radiation patterns are shown in Figure 16. The instrument responses have been deconvolved from the original recordings to obtain ground displacements and one time derivative was taken to obtain ground velocity. The data was then bandpassed between 0.1 to 1.0 Hz.

For the teleseismic data, we predicted the first 25 sec of the *P* wavetrains based on the strong motion slip model. The *P* waves were aligned in time by picking the first arrival, which were normally quite impulsive.

Comparison of the predicted teleseismic *P* waveforms with the observations (Figures 17a and 17b) suggests the slip model derived from strong-motion data alone adequately predicts both the amplitude and dominant waveform characteristics of the teleseismic data. Note that while the broadband displacements (Figure 17a) fit very well, the mismatch in the details of the higher-frequency velocity waveforms (Figure 17b) indicates that there is room for improvement in either or both the slip model and the teleseismic Green's functions.

CONCLUSIONS

A summary of the fault parameters determined from our study is presented in Table 4. The rupture began at a depth of 18.5 km and propagated predominantly in the updip direction approximately along the direction of the rake vector (109°). Slip terminated at a depth of about 7-8 km. Rupture occurred over an area approximately 14 km along strike (west-northwest from the hypocenter) and nearly 20 km updip. Our estimate of the seismic moment is $1.2 \pm \times 10^{26}$ dyne-cm with an average slip about 1.2 meters over the rupture area. The peak slip value is nearly 4 meters. Our estimate of the rupture velocity is 2.8 km/sec, though slightly faster rupture velocities give comparable solutions. The rise time is best approximated with durations less than about 1.2 sec.

The most robust features in our model, that is, those features found consistently over a wide range of input variables (e.g., rise time, rupture velocity, station weighting) include (1) substantial slip near the hypocenter, (2) slip updip and north of the hypocenter, enhancing the effects of directivity for the first subevent at stations updip and towards the north, (3) a secondary subevent in the form of a band of slip forming northwestern edge of the rupture (Figure 7), with substantial slip at the deepest portion of the fault and (4) short local slip

durations (less than 1.2 sec).

The up-dip, near-source strong-motion velocity waveforms show two distinct, large S-wave arrivals 2-3 sec apart, requiring separate subevents in our source model. This model also predicts the two arrivals observed on recordings to the south and southeast of the epicenter with time separations that are longer (about 4.5 sec at SCR and SHR, for example) than at northern azimuths. The correspondence to secondary arrivals observed at more distant stations to the south (e.g., Santa Monica) is more tenuous, since several of the aftershocks recorded there indicate later arrivals as well, but, clearly, a secondary source contribution is expected based on our model of the near-source stations.

Future work on the source process of the Northridge earthquake will include the addition of ground motion data not yet available, inclusion of the static displacements determined from GPS resurveys when that data is released, and the replacement of our simple 1-D Green's functions with those from 2- and perhaps 3-D earth structure approximations. We are in the process of analyzing aftershock recordings at sites that recorded the mainshock in an effort to (1) determine the level of complexity in the waveforms that is not addressed in our simple 1-D Green's functions and (2) determine suitable velocity structure modifications for improving the Green's function calculations.

ACKNOWLEDGEMENTS

Gene Hawkins of Southern California Edison and Ron Tognazinni, Craig Davis, Philip Lahr of the Los Angeles Department of Power and Water generously provided information and data from their strong-motion stations. Discussions with Doug Dreger, Rob Graves, Hong Kie Thio, and Leif Wennerberg were helpful. Reviews by Steve Hartzell and Lisa Wald the original manuscript.

REFERENCES

Abercrombie, R. E. and J. Mori (1994). Local observations of the onset of a large earthquake: 28 June 1992 Landers, California, *Bull. Seism. Soc. Am.*, **84**, 725-734.

Dreger, D. S. and D. V. Helmberger (1990). Broadband modeling of local earthquakes, *Bull. Seism. Soc. Am.*, **80**, 1162-1179.

Dreger, D. S. (1994). Empirical Green's function study of the January 17, 1994 Northridge Mainshock (M_W6.7), submitted to *Geophys. Res. Lett.*

Earthquake Engineering Research Institute (1992). EERI special Earthquake report, August 1992, *EERI Newsletter*, **26**, 1-12.

Ellsworth, W. L. and G. Beroza (1994). Nucleation and intial growth of the Northridge, California, earthquake, Program for Northridge abstracts, Seismo. Soc. of Am. Annual Meeting, Pasadena.

Frankel, A. (1994). Dense array recordings in the San Bernadino Valley of Landers-Big Bear aftershocks: basin surface waves, moho reflections, and three-dimensional simulations, *Bull. Seism. Soc. Am.*, **84**, 613-624.

Hartzell, S. H. and T. H. Heaton (1983). Inversion of strong ground motion and teleseismic waveform data for the fault rupture history of the 1979 Imperial Valley, California earthquake, *Bull. Seism. Soc Am.*, **73**, 1553-1583.

Heaton, T. H. (1982). The 1971 San Fernando earthquake: a double event?, *Bull. Seism. Soc. Am.*, **72**, 2037-2062.

Langston, C. A. (1978). The February 9, 1971 San Fernando earthquake: a study of source finiteness in teleseismic bodywaves, *Bull. Seism. Soc. Am.*, **68**, 1-29.

Langston, C. A. and D. V. Helmberger (1975). A procedure for modeling shallow dislocation sources, *Geophys. J.*, **42**, 117-130.

Liu, H.-L. and T. H. Heaton (1984). Array analysis of the ground velocities and accelerations from the 1971 San Fernando California earthquake, *Bull. Seism. Soc. Am.*, **74**, 1951-1968.

Mendoza, C. and S. H. Hartzell (1988). Aftershock patterns and main shock faulting, *Bull. Seism. Soc. Am.*, **78**, 1438-1449.

Olson A. H., J. Orcutt and G. Frazier (1984). The discrete wavenumber/finite element method for synthetic seismograms, *Geophys. J. R. Astr. Soc.* **77**, 421-460.

Porcella, R. L., E. C. Etheredge, R. P. Maley, and A. V. Acosta (1994). Accelerograms recorded at USGS national strong-motion network stations during the M_S = 6.6 Northridge, California earthquake of January 17, 1994, *U.S.G.S. Open-file Report*

94-141, 100 pp.

Shakal, A., M. Huang, R. Darragh, T. Cao, R. Sherburne, P. Malhotra, C. Cramer, R. Sydnor, V. Graizer, G. Maldonado, C. Peterson, and J. Wampole (1994). CSMIP strong motion records from the Northridge, California earthquake of 17 January, 1994. *Report No. OSMS 94-07, California Strong Motion Instrumentation Program*, 308 pp.

Thio, H. K. and H. Kanamori (1994). Source complexity of the 1994 Northridge earthquake and its relation to aftershock mechanisms, submitted to *Geophys. Res. Lett.*.

U.S. Geological Survey and the Southern California Earthquake Center (1994). The magnidue 6.7 Northridge, California, Earthquake of January 17, 1994, submitted to Science.

Vidale, J. E. and D. V. Helmberger (1988). Elastic finite difference modeling of the 1971 San Fernando, California earthquake, *Bull. Seism. Soc. Am.*, **78**, 122-141.

Wald, D. J. (1992). Strong Motion and Broadband Teleseismic Analysis of the 1991 Sierra Madre, California, Earthquake, *J. Geophys. Res.*, **97**, 11,033-11,046.

Wald, D. J. and T. H. Heaton (1994). Spatial and temporal distribution of slip for the 1992 Landers, California, earthquake, *Bull. Seism. Soc. Am.*, **84**, 668-691.

Wald, D. J., T. H. Heaton and D. V. Helmberger (1991). Rupture model of the 1989 Loma Prieta earthquake from the inversion of strong motion and broadband teleseismic data, *Bull. Seism. Soc. Am.*, **81**, 1540-1572.

TABLE 1. STRONG MOTION STATION INFORMATION

Abbrev.	No.	Station Name	N.Lat	W.Long	Epicentral Distance*	Trigger Time@	Codes#
ALHF		Alhambra Freemont School	34.070	118.150	39		DJ
ARL		Arleta - Nordhoff Ave. Fire Station	34.236	118.439	9		C
BLD		LA - Baldwin Hills	34.009	118.361	28		N
BUR		Burbank - 6-story Commercial Bldg.	34.185	118.308	22		N
CAS		Castaic Old Ridge Route	34.564	118.642	40	8.0	C
ECC		Energy Control Center	34.259	118.336	19		L
ELD		Castaic Elderberry Dam Right Abutment	34.562	118.628	40		LN
ENR		Encino Encino Reservoir Dam Abutment	34.15	118.51	7		L
GRF		Griffith Park Griffith Observatory	34.118	118.299	26		UN
HYSB		Los Angeles Hollywood Storage Bldg.	34.090	118.339	23		DJ
NHW		North Hollywood - 20-story Hotel	34.138	118.359	19	5.1	CN
UCL		Los Angeles - 7-story UCLA Math-Science Bldg.	34.069	118.442	19		CN
JFP		Granada Hills Jenson Filtr. Plant Generator Bld.	34.312	118.496	12		U
LADM		Sylmar Los Angeles Dam Right Abutment	34.294	118.483	11		LN
LH9		Lake Hughes #9	34.608	118.558	44	5.0	C
MNG		Monte Nido Fire Station	34.078	118.693	21		U
MOR		Moorpark	34.288	118.881	33	7.3	C
NHL		Newhall LA County Fire Dept	34.387	11.530	20		C
PARD		Santa Clarita Pardee Substation	34.435	118.582	25		E
PDM		Pacoima Dam Downstream	34.334	118.396	19		C

PIRU	Lake Piru Santa Felicia Dam Downstream	34.460 118.753	34	7.5	C
PKC	Pacoima - Kagel Canyon Fire Sta. #74	34.288 118.375	17	4.1	C
PTDM	Malibu Point Dume	34.013 118.800	32	6.6	CN
PTMG	Point Mugu Laguna Peak	34.109 119.065	50	10.9	CN
RRS	Sylmar Rinaldi Receiving Station	34.281 118.479	9		LF
RSE	San Fernando Receiving Station East	34.17 118,36	17		L
SCC	Sepulvada Canyon Control Facility	34.097 118.478	15		U
SCR	Stone Canyon Reservoir site	34.106 118.454	24		DJ
SCS	Sylmar Sylmar Converting Station	34.312 118.481	12		L
SMC	Santa Monica - City Hall Grounds	34.011 118.490	24	7.5	C
SVA	Supulveda V.A. Hospital	34.312 118.475	8		C
SSU	Santa Susanna D.O.E. - Ground Site	34.230 118.713	16		U
SYL	Sylmar - 6-story County Hospital Parking Lot	34.326 118.444	15	5.0	C
TPG	Topanga Fire Station	34.084 118.600	16		U
VNY	Van Nuys - 7-story Hotel	34.221 118.471	6		CN
VSQZ	Vasquez Rocks Park	34.490 118.320	39	7.3	C
WOOD	Wood Ranch Dam	34.240 118.820	26	6.2	C
WVA	Wadsworth V.A. Hospital	34.052 118.451	19		UN

---

* Approximate distance in km from estimated epicenter at 34.219N, 118.538W

@ Trigger time after origin time of 12:30 55.2 (when known)

Codes: D=Digital; N=Not Used in Invserion, C=C.D.M.G., U=U.S.G.S, =U.C.S.B, E=So. Cal. Edison, L=L.A. Dept. Water and Power.

TABLE 2. STRONG-MOTION STATIONS: TRIGGER TIMES

STATION	DISTANCE	P PRED#	P TRIG%	TRIG TIME USED*
ARL	9.48	3.70	-	4.28
CAS	40.30	7.59	8.20	7.80
ECC	19.31	4.70	-	5.92
ENR	7.23	3.55	-	4.40
JFP	11.82	3.90	-	4.44
MNG	20.59	4.85	-	5.90
MOR	32.77	6.49	7.50	7.70
NHL	19.85	4.76	4.80	5.10
NH20	18.35	4.58	5.30	5.60
PAR	25.16	5.44	-	5.40
PDM	18.85	4.64	-	5.55
PIRU	33.99	6.67	7.70	8.40
PKC	17.22	4.45	4.30	5.40
RRS	9.44	3.70	-	5.06
RSE	16.82	4.41	-	4.91
SCC	13.80	4.09	-	4.51
SCR	13.98	4.11	-	4.20
SCS	12.34	3.95	-	4.40
SHR	9.21	3.68	-	4.48
SSU	16.31	4.35	-	5.34
SVA	12.58	3.97	-	4.10
SYL	15.38	4.25	5.20	5.00
TPG	15.24	4.24	-	4.86
VNY	6.22	3.49	-	3.79
VSQZ	36.84	7.08	7.50	8.20
WOOD	26.23	5.58	6.40	6.40

Predicted P arrival after time after 12:30 55.2 GMT
% Observed Trigger time when known
* Trigger time used in source inversion for waveform alignment

TABLE 3. Teleseismic Station Parameters

STATION	AZIMUTH (Deg)	BACK AZIMUTH (Deg)	DISTANCE (Deg)
COL	-21.0	135.7	35.4
ESK	32.2	-50.7	74.9
GUMO	-75.1	55.3	87.7
HNR	-102.6	54.9	88.4
HRV	62.9	-86.9	37.3
MAJO	-52.7	55.0	79.5
OBN	13.9	-20.4	88.2
RAR	-138.4	36.0	67.9
SJG	95.2	-60.0	49.1
PAB	44.6	-49.1	84.4
KEV	11.8	-29.3	73.1

TABLE 4. Preferred Northridge Rupture Model Parameters

Date	January 17, 1994
Origin Time	12:30 55.2 GMT
Latitude, Longitude	34.211 N, 118.537 W
Hypocentral Depth	18.5 km
Top Center Fault Location	34.344 N, 118.517 W
Seismic Moment	1.23 x 10**26 dyne-cm
Strike	122 (S58W)
Dip	42 (S32W)
Rake	109
Model Fault Length	18 km
Model Fault Width	21 km
Effective Fault Length	14 km
Effective Fault Width	20 km
Fault Depth Range	6.0 - 20.0 km
Average Slip	1.2 meters
Maximum Slip	3.9 meters
Effective Rupture Area	280 square km
Rupture Velocity	2.8 km/sec
Total Rupture Time	7 sec
Local Rise Time	variable from 0.6-1.2 sec

TABLE 5. Preferred Rupture Model Slip Values*

---

14 subfaults downdip (rows), 14 subfaults along strike (columns) in SPYGLASS "special ascii" format. Left = Northwest, Right = Southeast. The hypocenter is in the subfault with 3.94 meters of slip. The 2nd line indicates slip minimum and maximum slip values.

```
14  14
0.0 3.94
6.5,7.5,8.5,9.5,10.5,11.5,12.5,13.5,14.5,15.5,16.5,17.5,18.5,19.5
.64,1.93,3.2,4.5,5.79,7.07,8.36,9.64,10.93,12.2,13.5,14.8,16.07,17.36

0.00,1.01,0.80,0.00,1.06,0.79,1.61,0.88,0.00,0.00,0.34,0.39,0.09,0.00
0.00,1.07,0.82,0.37,0.00,1.96,2.60,0.74,0.08,0.19,0.38,0.40,0.06,0.19
0.06,0.87,1.19,0.00,0.74,2.95,0.93,0.00,0.00,0.00,0.00,0.00,0.18,1.09
0.00,0.74,0.08,0.00,2.03,1.57,0.00,0.00,0.00,0.28,0.45,0.00,0.00,0.00
0.00,0.51,0.00,0.47,2.20,0.84,0.00,0.00,1.21,1.68,1.21,0.79,0.63,0.40
0.00,0.00,0.00,1.42,2.13,0.00,0.00,0.95,1.52,1.24,1.24,1.38,0.90,0.00
0.00,0.00,0.60,1.47,1.33,0.00,0.91,1.75,1.68,1.52,1.63,1.15,0.31,0.00
0.00,0.08,0.79,1.60,1.05,0.00,1.25,2.21,2.29,2.33,1.77,0.85,0.35,0.23
0.00,0.14,0.88,1.91,0.73,0.00,2.14,2.92,2.60,2.17,1.47,0.90,0.53,0.63
0.00,0.00,0.96,2.04,0.53,0.00,2.82,2.62,2.15,2.17,2.33,1.80,0.39,0.00
0.16,0.12,0.92,2.31,0.79,0.06,1.88,1.42,1.13,1.62,2.76,2.66,0.94,0.00
0.13,0.53,0.67,2.56,1.59,0.46,0.44,0.37,0.56,1.68,3.45,3.11,1.04,0.00
0.00,0.69,0.66,2.19,2.75,1.30,0.00,0.00,0.71,1.75,2.99,3.94,1.44,0.00
0.08,0.30,1.33,0.84,3.20,1.81,1.01,0.00,0.43,1.52,1.08,0.95,0.00,0.00
```

---

* Available through E-mail: send request to wald@seismo.gps.caltech.edu

FIGURES

Fig. 1. Map view and cross-section (right) of the aftershock distribution for the Northridge earthquake from January 17-31, 1994 (courtesy of E. Hauksson). The thick line indicates the dimensions of the fault plane used in this study.

Fig. 2. Velocity structure model used to compute the strong-motion Green's functions (modified from Langston, 1978, Model C).

Fig. 3. Plot of predicted P wave arrival times verses observed trigger times. The short-dashed line represents the predicted P arrival time plus a delay of 0.5 sec.

Fig. 4. Location map displaying the strong-motion stations examined in this study. The epicenter is marked by a star. Shaded areas represent alluvial basins and valleys.

Fig. 5. (a) Distribution of ground motions for select strong-motion stations shown in map view. Time histories are plotted close to the associated site. Time and amplitude scales are shown to the right. Shaded areas represent alluvial basins and valleys. (a) North component of acceleration. (b) East component of acceleration. (c) North component of velocity. (d) East component of velocity. (e) North component of bandpassed velocity. (f) East component of bandpassed velocity.

Fig. 6. Comparison of the observed (top) and synthetic (bottom) ground velocities. For each station, the first pair of records are the observed and synthetic north component, followed by the observed and synthetic east and vertical components.

Fig. 7. Cross-section of the slip distribution determined from modeling the strong motion data with a single time window (top). The view is from the southwest and above the fault plane. The contour interval is 1 meter and the first contour given is 0.5 meters. The scale bar to the right of each fault shows the slip shading in meters. Gridding displays the subfault layout. Concentric circles depict the advance of the rupture front at 1 sec intervals. The lower portion of the figure indices the rake direction and the relative sip amplitude on each subfault.

Fig. 8. Cross-section of the slip distribution determined from modeling the strong-motion data with three time windows (top). Otherwise, same as Figure 7.

Fig. 9. Individual time window contributions for the three-time-window slip model. The time above each window gives the duration (see text for details). The contour interval is 0.5 meters.

Fig. 10. Time progression of the Northridge rupture model given at intervals of 1 sec as labeled. The contour interval is 0.5 m.

Fig. 11. (a) Comparison of data (top trace) and synthetics (second trace) with contributions to the synthetics from regions S1 (third trace) and S2 (fourth trace) on the fault for stations JFP and PDM. (b) Same for stations SSU and VNY.

Fig. 12. Comparison of the 1989 Loma Prieta, 1991 Sierra Madre, 1992 Landers, and 1994 Northridge slip models plotted on the same scale. The Landers contour interval is 1 meter; all others are 0.5 meters.

Fig. 13. Cross-section (top) of the 1971 San Fernando (blue) and 1994 Northridge (red) aftershock distributions with solid lines depicting the fault planes. Lower figure shows a map view of the aftershock distributions with the slip contours for the Northridge and San Fernando earthquakes superimposed. The contour interval is 1.0 meters, with the first contour value at 0.5 meters. Aftershock distribution figure courtesy of J. Mori and 1971 slip distribution is modified from Heaton (1982).

Fig. 14. Map illustrating the grid of stations and the contoured distribution of peak ground velocities from the strong-motion forward prediction. Contour interval is 10 cm/sec.

Fig. 15. Map indicating variability of predicted velocity waveforms as a function of location. Amplitude and time scales are shown at the right. (a) North components. (b) East components.

Fig. 16. Global station distribution for teleseismic records shown by take-off and azimuth angles plotted on focal spheres.

Fig. 17. Comparison of observed (top) and synthetic (bottom) teleseismic vertical P wave (a) displacement and (b) velocity records as predicted from the strong-motion rupture model.

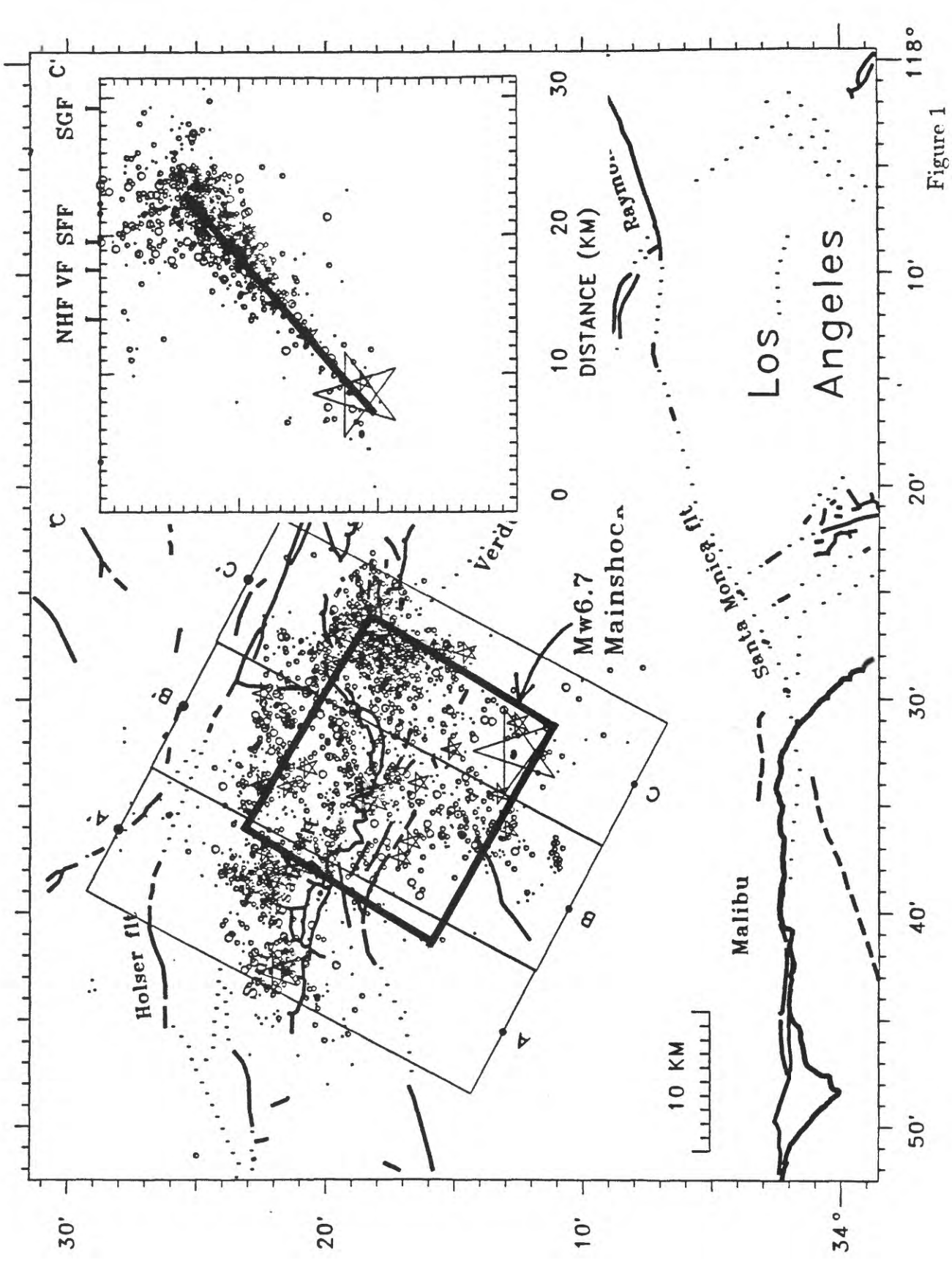
NHF VF SFF SGF
C'
C
DISTANCE (KM)
Mw6.7
Mainshock
Holser fl
Santa Monica fl
Malibu
Los
Angeles
10 KM
34°
30'
20'
10'
50'
40'
30'
20'
10'
118°

Figure 1

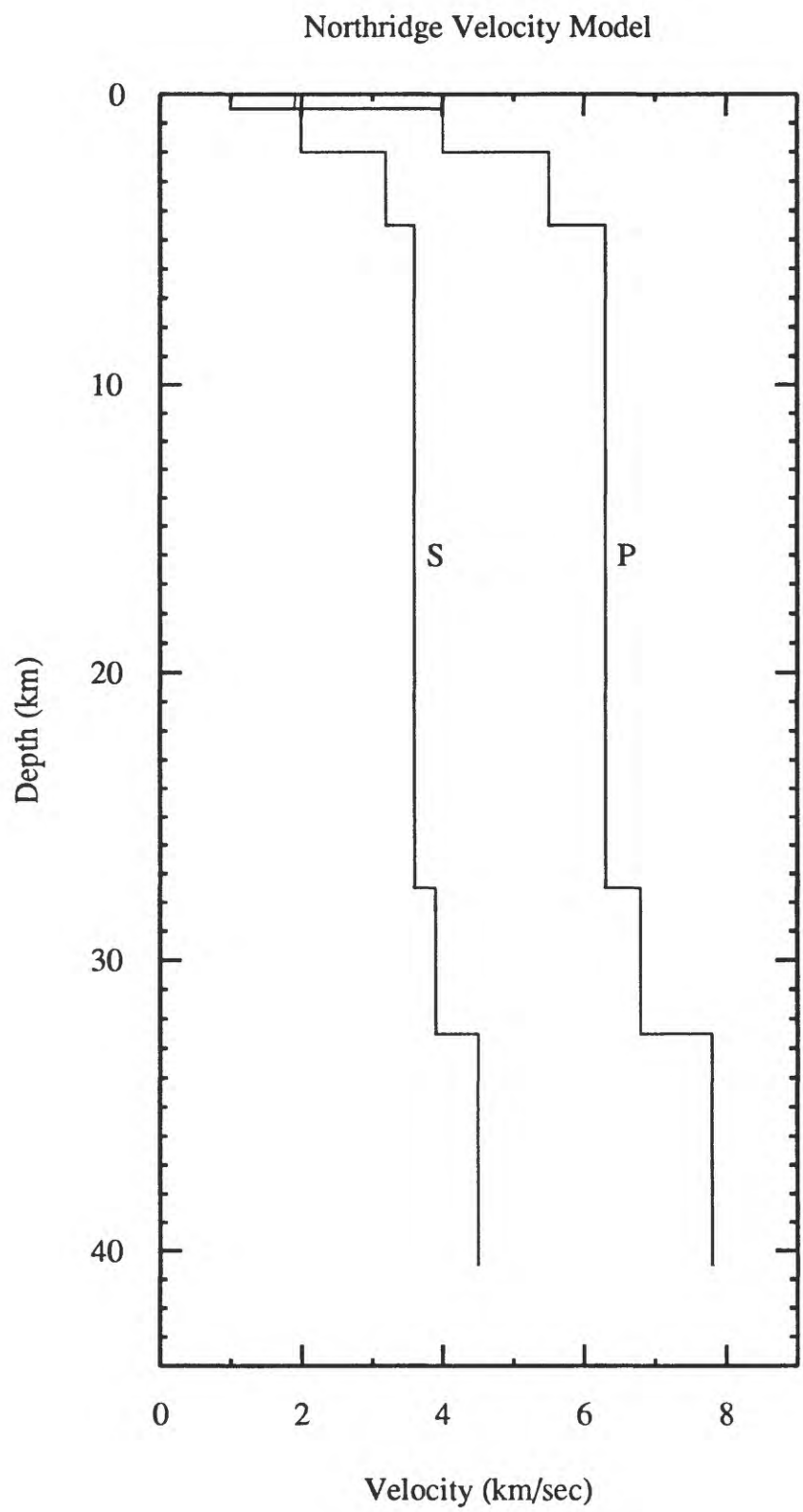
Northridge Velocity Model
0
10
20
30
40
Depth (km)
S
P
0
2
4
6
8
Velocity (km/sec)

Figure 2

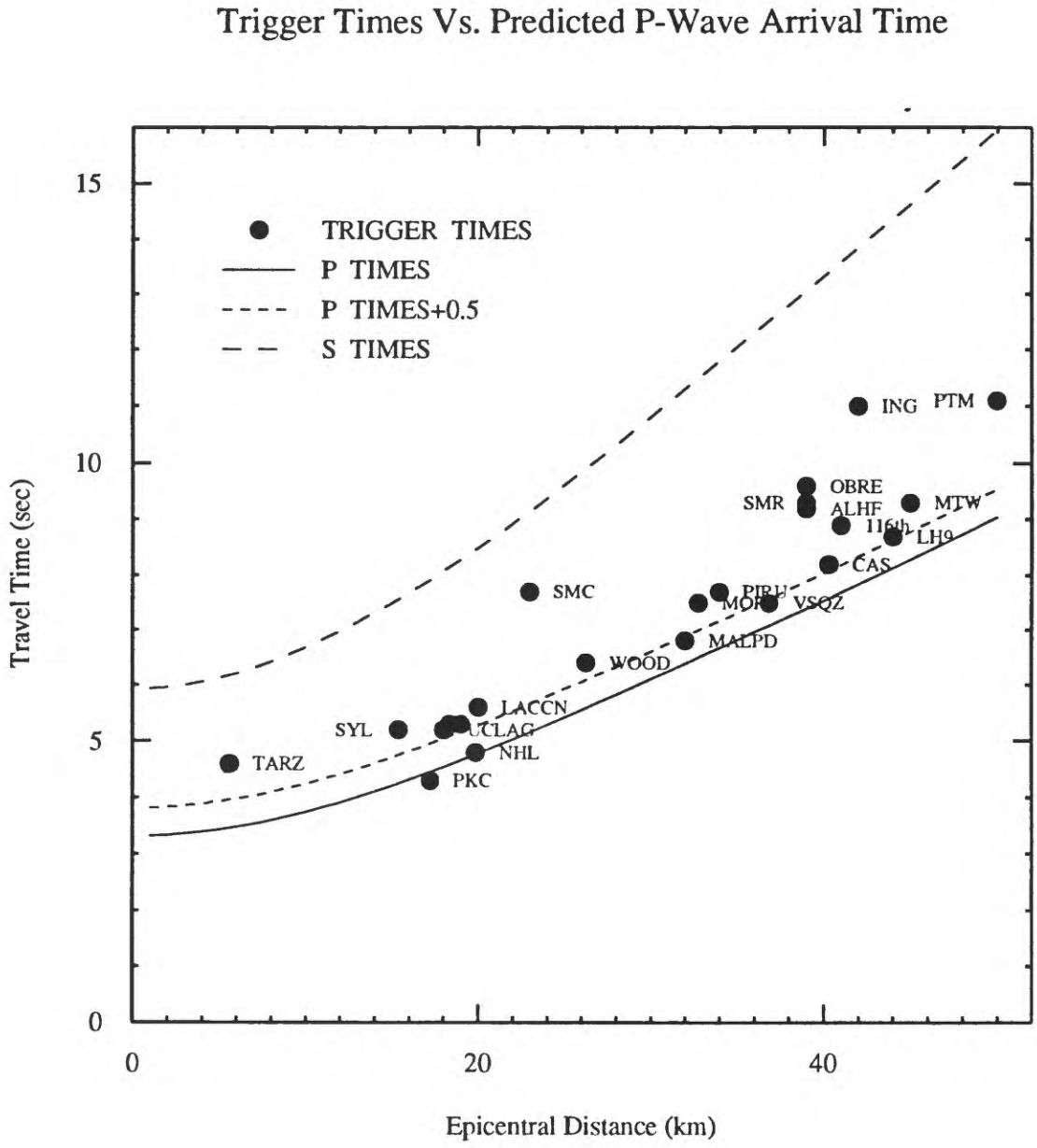
Trigger Times Vs. Predicted P-Wave Arrival Time
TRIGGER TIMES
P TIMES
P TIMES+0.5
S TIMES
ING
PTM
OBRE
SMR
ALHF
MTW
LH9
CAS
SMC
VSQZ
MALPD
WOOD
LACCN
SYL
UCLAG
NHL
TARZ
PKC
Travel Time (sec)
Epicentral Distance (km)
0
5
10
15
0
20
40

Figure 3

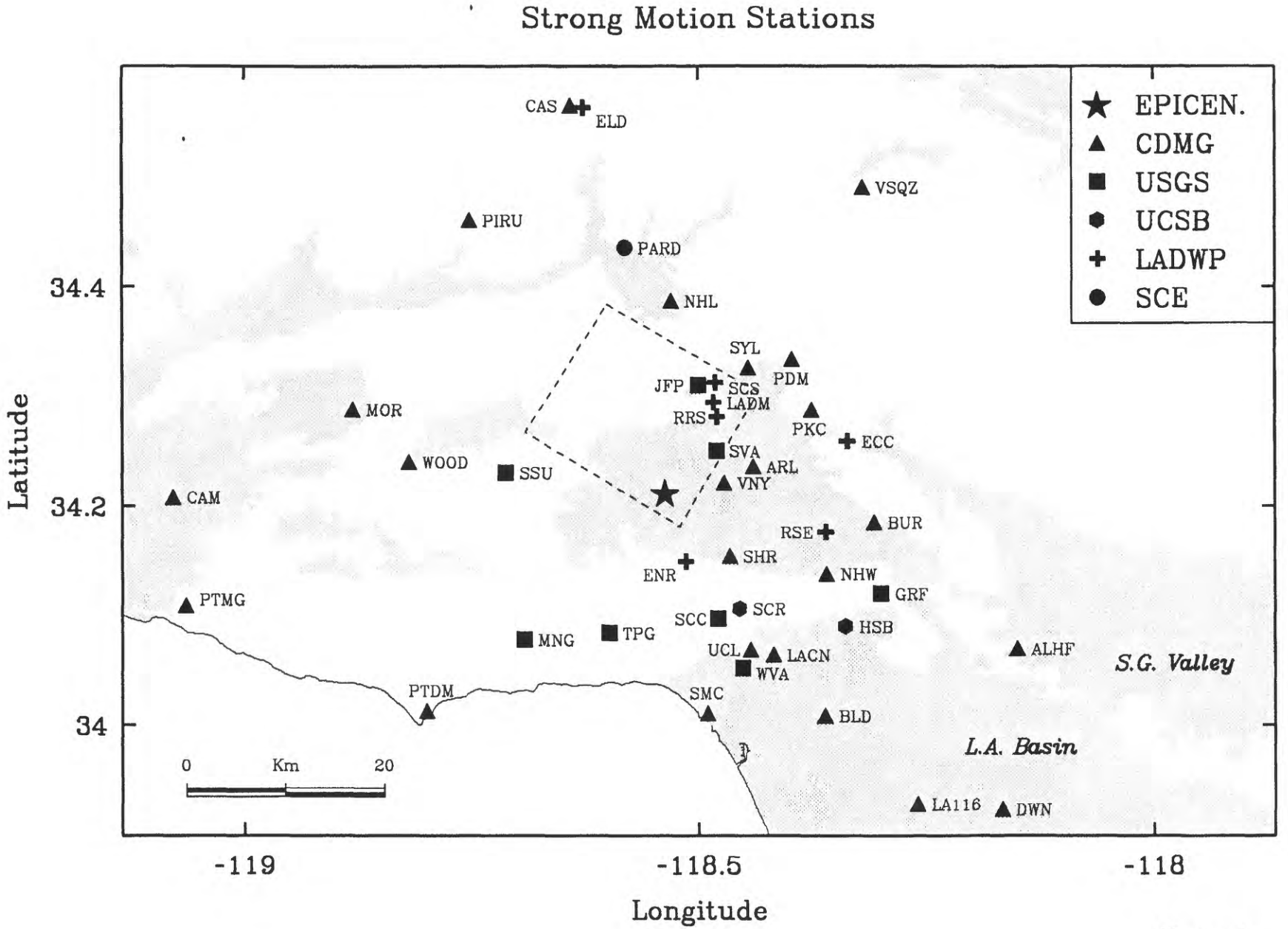
Strong Motion Stations
EPICEN.
CDMG
USGS
UCSB
LADWP
SCE
CAS
ELD
VSQZ
PIRU
PARD
NHL
SYL
PDM
JFP
SCS
LADM
RRS
PKC
ECC
MOR
SVA
ARL
WOOD
SSU
VNY
CAM
RSE
BUR
SHR
ENR
NHW
GRF
PTMG
SCC
SCR
HSB
MNG
TPG
UCL
LACN
WVA
ALHF
S.G. Valley
PTDM
SMC
BLD
L.A. Basin
0
Km
20
LA116
DWN
34.4
34.2
34
-119
-118.5
-118
Latitude
Longitude

Figure 4

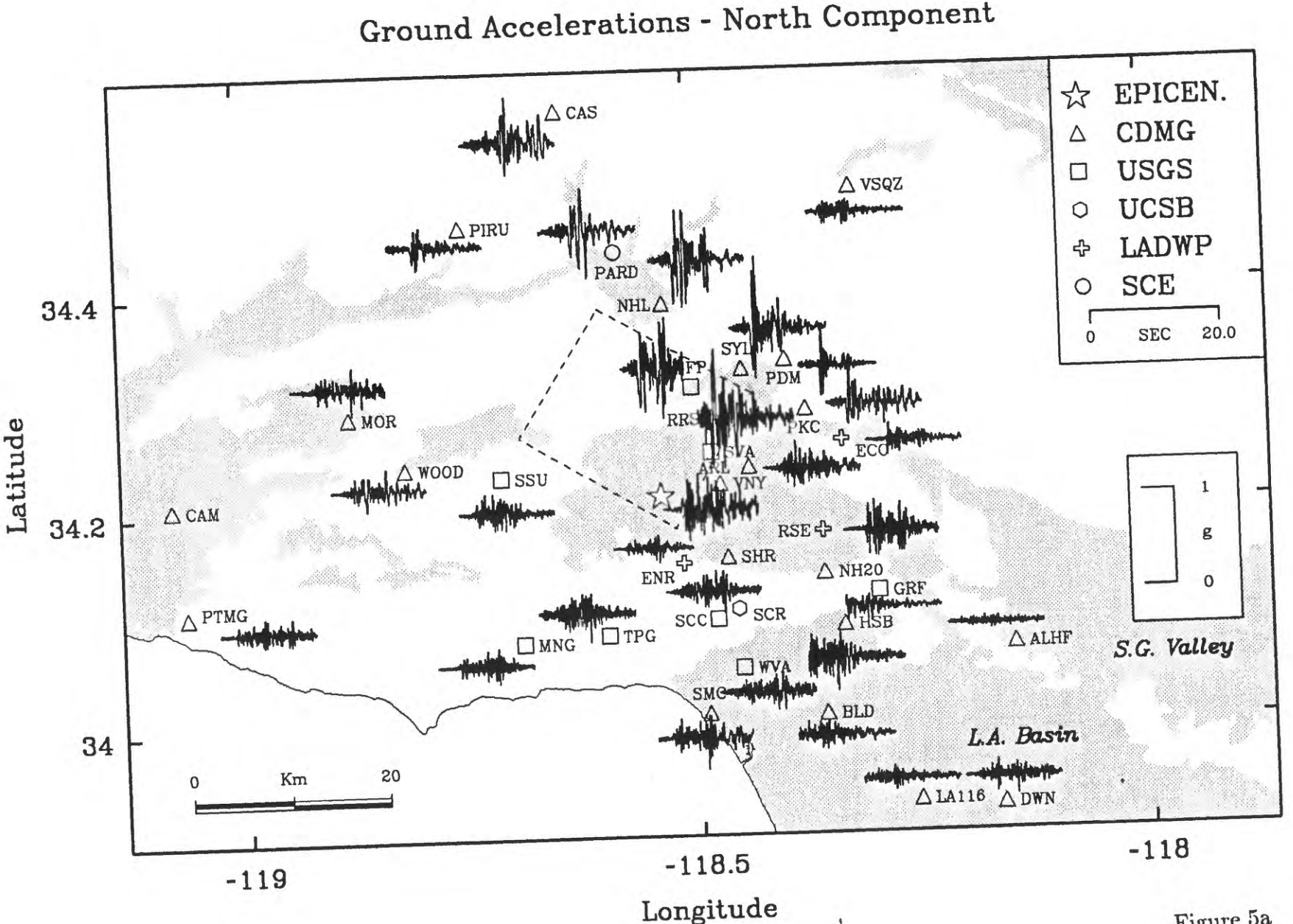
Ground Accelerations - North Component
EPICEN.
CDMG
USGS
UCSB
LADWP
SCE
0 SEC 20.0
1
g
0
CAS
VSQZ
PIRU
PARD
NHL
SYL
FP
PDM
MOR
RRS
KC
ECO
VA
ARL
YNY
WOOD
SSU
CAM
RSE
SHR
ENR
NH20
GRF
SCC
SCR
HSB
PTMG
MNG
TPG
ALHF
WVA
SMC
BLD
S.G. Valley
L.A. Basin
LA116
DWN
0 Km 20
34.4
34.2
34
-119
-118.5
-118
Latitude
Longitude

Figure 5a

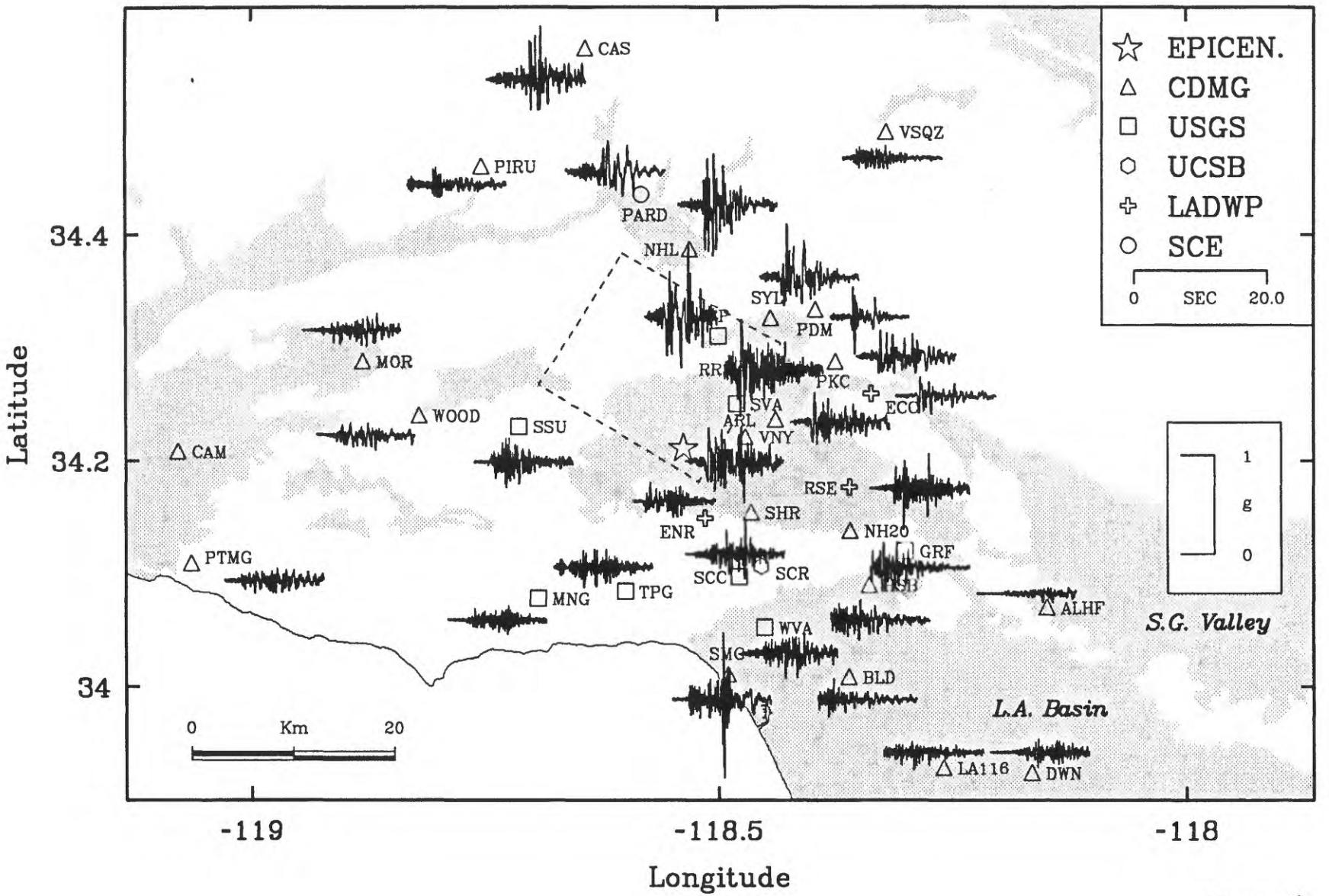
Ground Accelerations - East Component
EPICEN.
CDMG
USGS
UCSB
LADWP
SCE
0 SEC 20.0
1
g
0
CAS
VSQZ
PIRU
PARD
NHL
SYL
PDM
MOR
RR
PKC
WOOD
SSU
SVA
ECO
ARL
VNY
CAM
RSE
SHR
ENR
NH20
GRF
PTMG
SCC
SCR
MNG
TPG
ALHF
WVA
SMG
BLD
S.G. Valley
L.A. Basin
LA116
DWN
0 Km 20
34.4
34.2
34
-119
-118.5
-118
Latitude
Longitude

Figure 5b

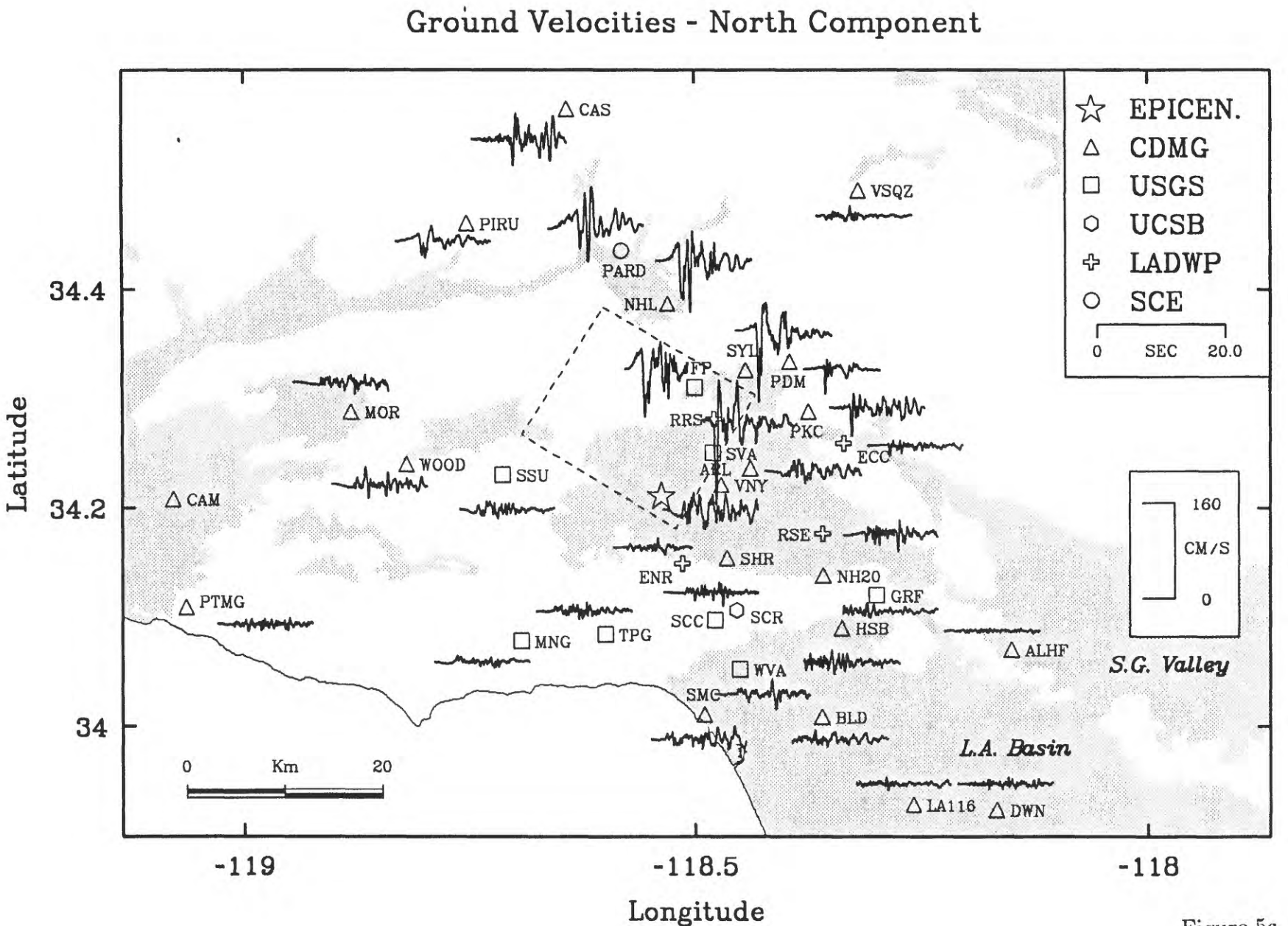
Ground Velocities - North Component
EPICEN.
CDMG
USGS
UCSB
LADWP
SCE
0 SEC 20.0
160
CM/S
0
CAS
PIRU
VSQZ
PARD
NHL
SYL
FP
PDM
MOR
RRS
PKC
ECC
WOOD
SSU
SVA
ARL
VNY
CAM
RSE
SHR
ENR
NH20
GRF
PTMG
SCC
SCR
HSB
MNG
TPG
ALHF
WVA
SMC
BLD
S.G. Valley
L.A. Basin
LA116
DWN
0 Km 20
34.4
34.2
34
-119
-118.5
-118
Latitude
Longitude

Figure 5c

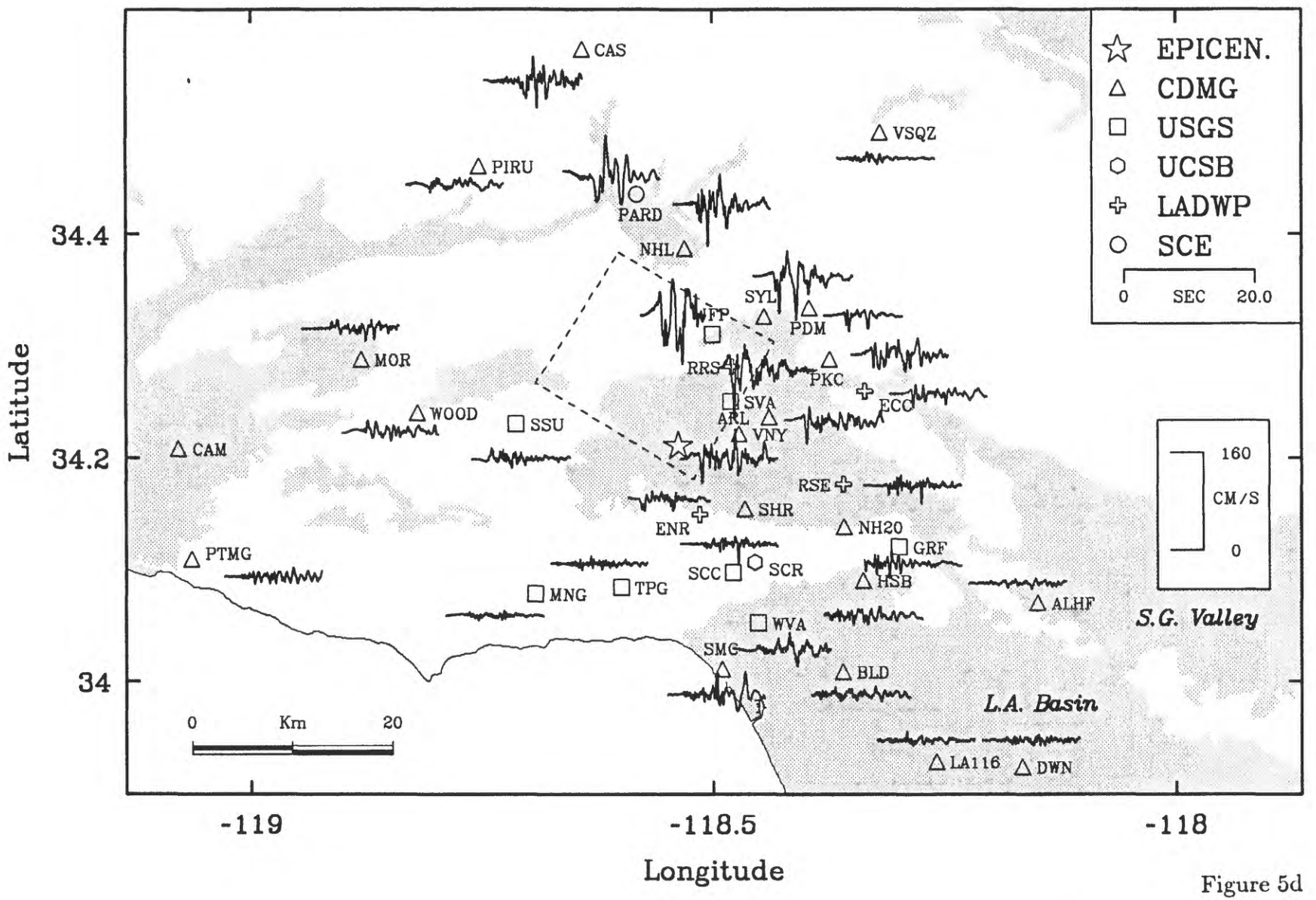
Ground Velocities - East Component
EPICEN.
CDMG
USGS
UCSB
LADWP
SCE
0 SEC 20.0
160
CM/S
0
CAS
VSQZ
PIRU
PARD
NHL
SYL
FP
PDM
MOR
RRS
PKC
SVA
ECC
WOOD
SSU
ARL
VNY
CAM
RSE
SHR
ENR
NH20
GRF
PTMG
SCC
SCR
HSB
MNG
TPG
ALHF
WVA
SMG
BLD
S.G. Valley
L.A. Basin
LA116
DWN
0 Km 20
34.4
34.2
34
-119
-118.5
-118
Latitude
Longitude

Figure 5d

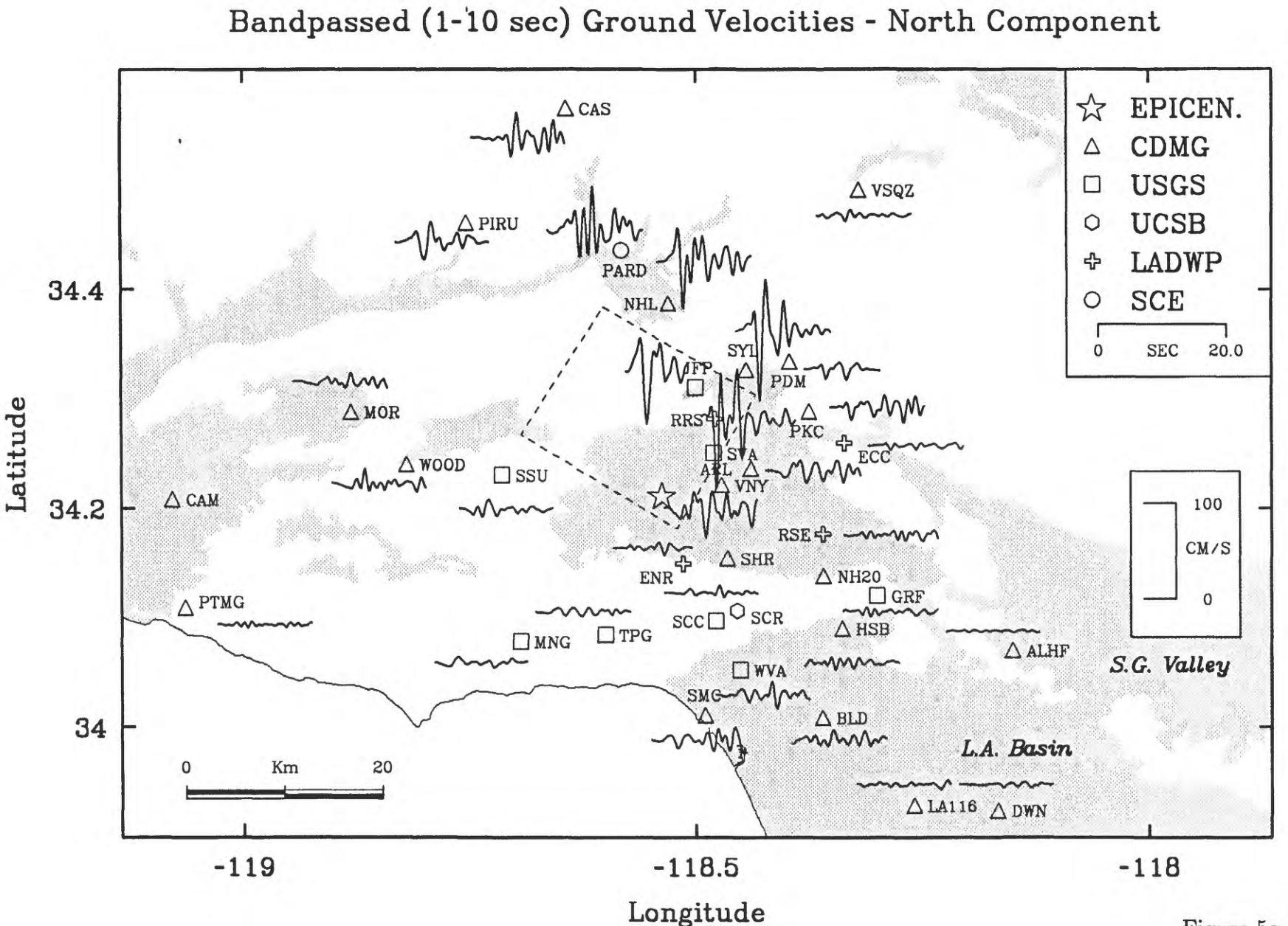
Bandpassed (1-10 sec) Ground Velocities - North Component
EPICEN.
CDMG
USGS
UCSB
LADWP
SCE
0 SEC 20.0
100
CM/S
0
CAS
VSQZ
PIRU
PARD
NHL
SYL
FP
PDM
MOR
RRS
PKC
ECC
WOOD
SSU
SVA
ATL
VNY
CAM
RSE
SHR
ENR
NH20
GRF
PTMG
SCC
SCR
HSB
MNG
TPG
ALHF
WVA
SMG
BLD
S.G. Valley
L.A. Basin
LA116
DWN
0 Km 20
34.4
34.2
34
-119
-118.5
-118
Latitude
Longitude

Figure 5e

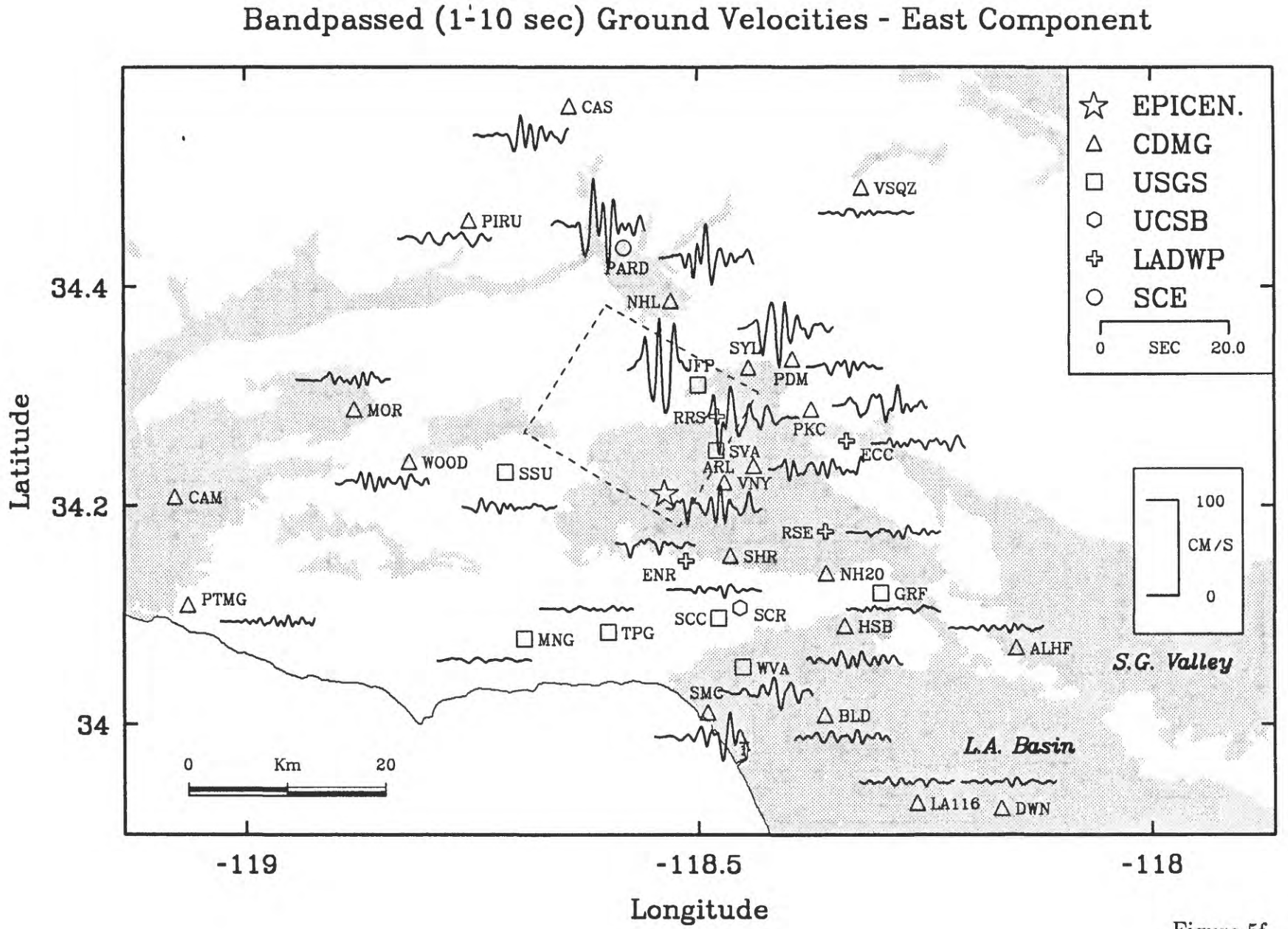
Bandpassed (1-10 sec) Ground Velocities - East Component
EPICEN.
CDMG
USGS
UCSB
LADWP
SCE
0 SEC 20.0
100
CM/S
0
CAS
VSQZ
PIRU
PARD
NHL
SYL
PDM
JFP
MOR
RRS
PKC
ECC
SVA
ARL
VNY
WOOD
SSU
CAM
RSE
SHR
ENR
NH20
GRF
PTMG
SCC
SCR
HSB
MNG
TPG
ALHF
WVA
SMC
BLD
S.G. Valley
L.A. Basin
LA116
DWN
0 Km 20
34.4
34.2
34
-119
-118.5
-118
Latitude
Longitude

Figure 5f

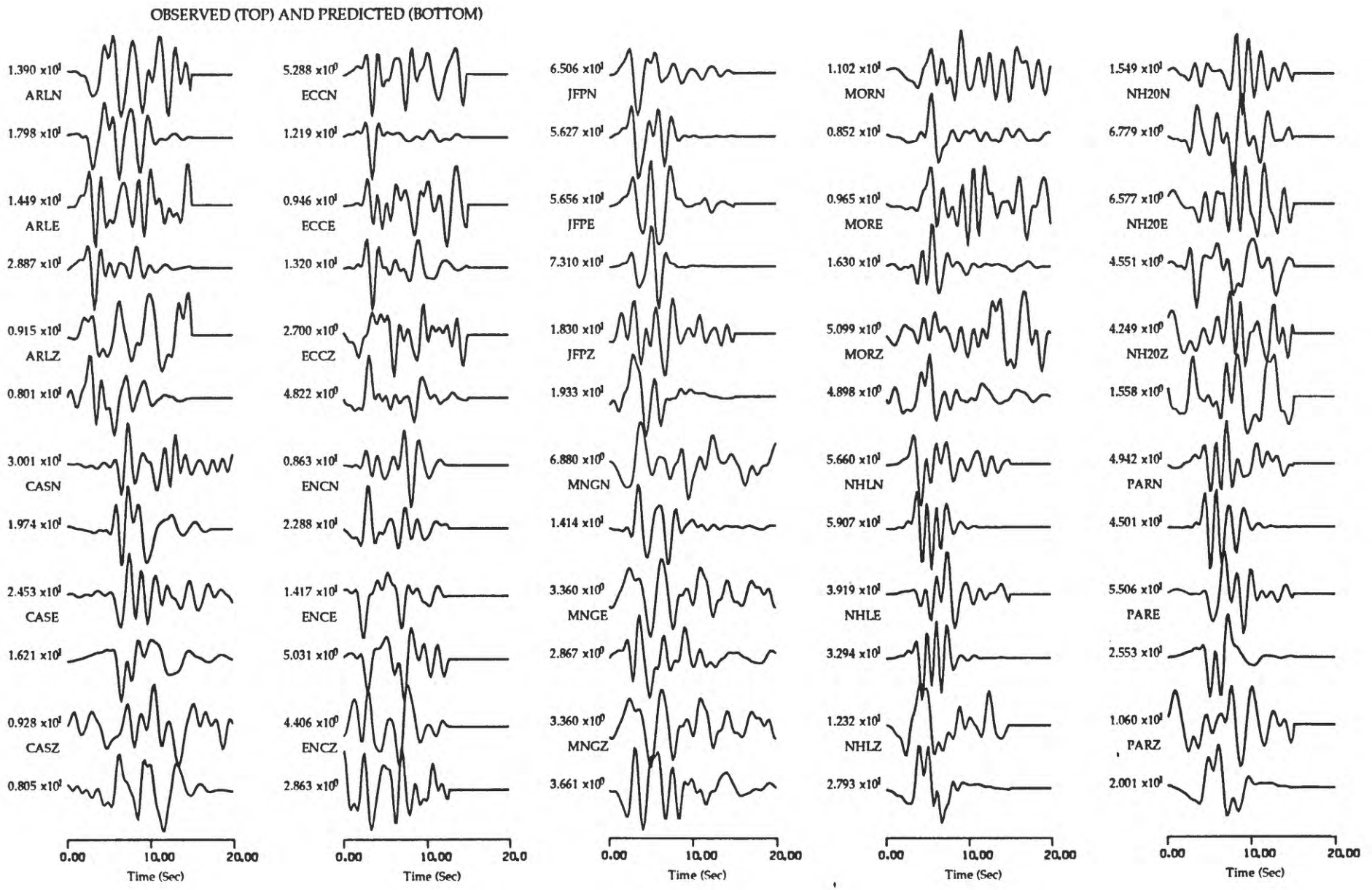
OBSERVED (TOP) AND PREDICTED (BOTTOM)
1.390 x10^1
ARLN
1.798 x10^1
1.449 x10^1
ARLE
2.887 x10^1
0.915 x10^1
ARLZ
0.801 x10^1
3.001 x10^1
CASN
1.974 x10^1
2.453 x10^1
CASE
1.621 x10^1
0.928 x10^1
CASZ
0.805 x10^1
0.00
10.00
20.00
Time (Sec)
5.288 x10^0
ECCN
1.219 x10^1
0.946 x10^1
ECCE
1.320 x10^1
2.700 x10^0
ECCZ
4.822 x10^0
0.863 x10^1
ENCN
2.288 x10^1
1.417 x10^1
ENCE
5.031 x10^0
4.406 x10^0
ENCZ
2.863 x10^0
0.00
10.00
20.0
Time (Sec)
6.506 x10^1
JFPN
5.627 x10^1
5.656 x10^1
JFPE
7.310 x10^1
1.830 x10^1
JFPZ
1.933 x10^1
6.880 x10^0
MNGN
1.414 x10^1
3.360 x10^0
MNGE
2.867 x10^0
3.360 x10^0
MNGZ
3.661 x10^0
0.00
10.00
20.00
Time (Sec)
1.102 x10^1
MORN
0.852 x10^1
0.965 x10^1
MORE
1.630 x10^1
5.099 x10^0
MORZ
4.898 x10^0
5.660 x10^1
NHLN
5.907 x10^1
3.919 x10^1
NHLE
3.294 x10^1
1.232 x10^1
NHLZ
2.793 x10^1
0.00
10.00
20.00
Time (Sec)
1.549 x10^1
NH20N
6.779 x10^0
6.577 x10^0
NH20E
4.551 x10^0
4.249 x10^0
NH20Z
1.558 x10^0
4.942 x10^1
PARN
4.501 x10^1
5.506 x10^1
PARE
2.553 x10^1
1.060 x10^1
PARZ
2.001 x10^1
0.00
10.00
20.00
Time (Sec)

Figure 6

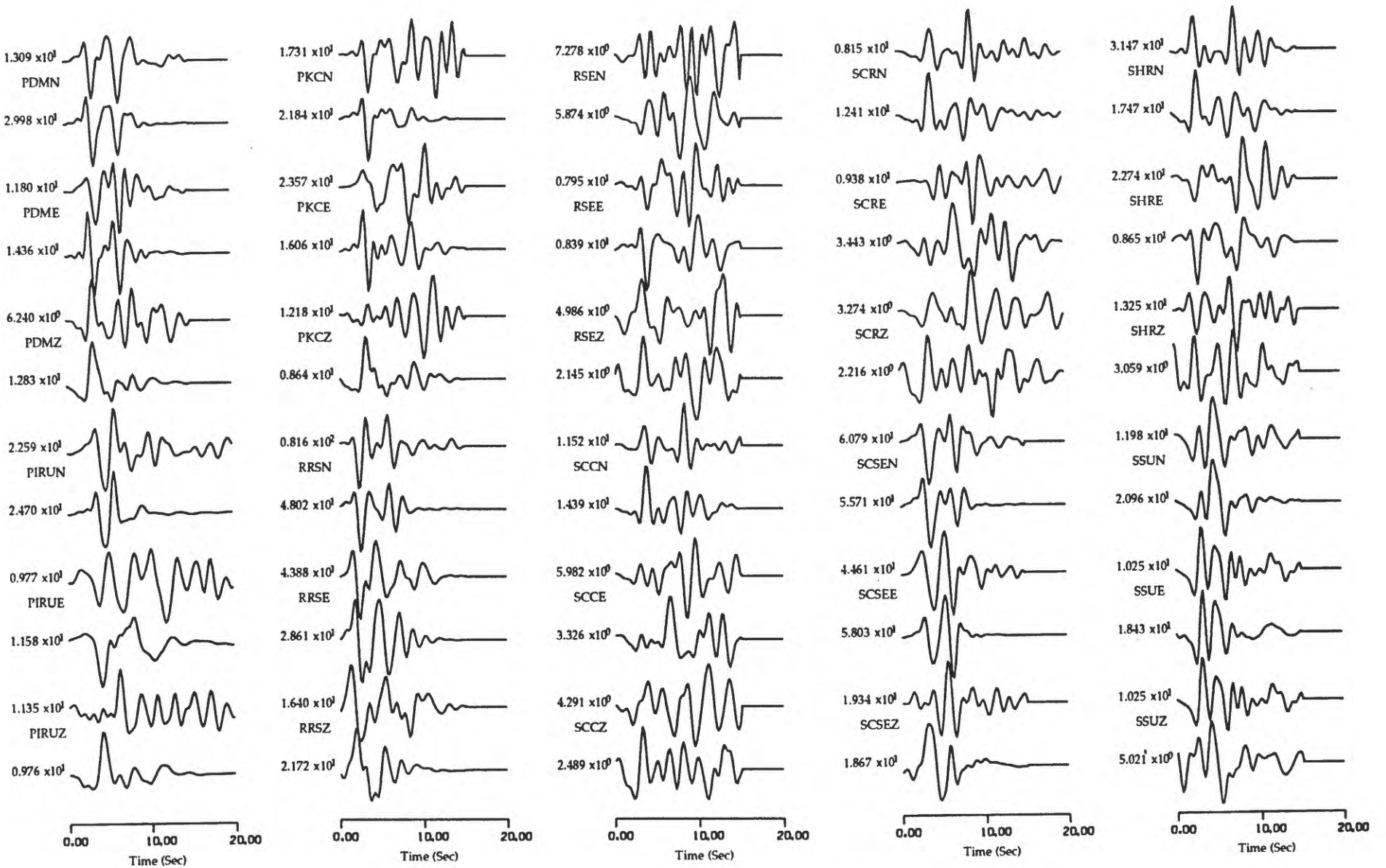
1.309 x10¹
PDMN
2.998 x10¹
1.180 x10¹
PDME
1.436 x10¹
6.240 x10⁰
PDMZ
1.283 x10¹
2.259 x10¹
PIRUN
2.470 x10¹
0.977 x10¹
PIRUE
1.158 x10¹
1.135 x10¹
PIRUZ
0.976 x10¹
0.00
10.00
20.00
Time (Sec)
1.731 x10¹
PKCN
2.184 x10¹
2.357 x10¹
PKCE
1.606 x10¹
1.218 x10¹
PKCZ
0.864 x10¹
0.816 x10²
RRSN
4.802 x10¹
4.388 x10¹
RRSE
2.861 x10¹
1.640 x10¹
RRSZ
2.172 x10¹
0.00
10.00
20.00
Time (Sec)
7.278 x10⁰
RSEN
5.874 x10⁰
0.795 x10¹
RSEE
0.839 x10¹
4.986 x10⁰
RSEZ
2.145 x10⁰
1.152 x10¹
SCCN
1.439 x10¹
5.982 x10⁰
SCCE
3.326 x10⁰
4.291 x10⁰
SCCZ
2.489 x10⁰
0.00
10.00
20.00
Time (Sec)
0.815 x10¹
SCRN
1.241 x10¹
0.938 x10¹
SCRE
3.443 x10⁰
3.274 x10⁰
SCRZ
2.216 x10⁰
6.079 x10¹
SCSEN
5.571 x10¹
4.461 x10¹
SCSEE
5.803 x10¹
1.934 x10¹
SCSEZ
1.867 x10¹
0.00
10.00
20.00
Time (Sec)
3.147 x10¹
SHRN
1.747 x10¹
2.274 x10¹
SHRE
0.865 x10¹
1.325 x10¹
SHRZ
3.059 x10⁰
1.198 x10¹
SSUN
2.096 x10¹
1.025 x10¹
SSUE
1.843 x10¹
1.025 x10¹
SSUZ
5.021 x10⁰
0.00
10.00
20.00
Time (Sec)

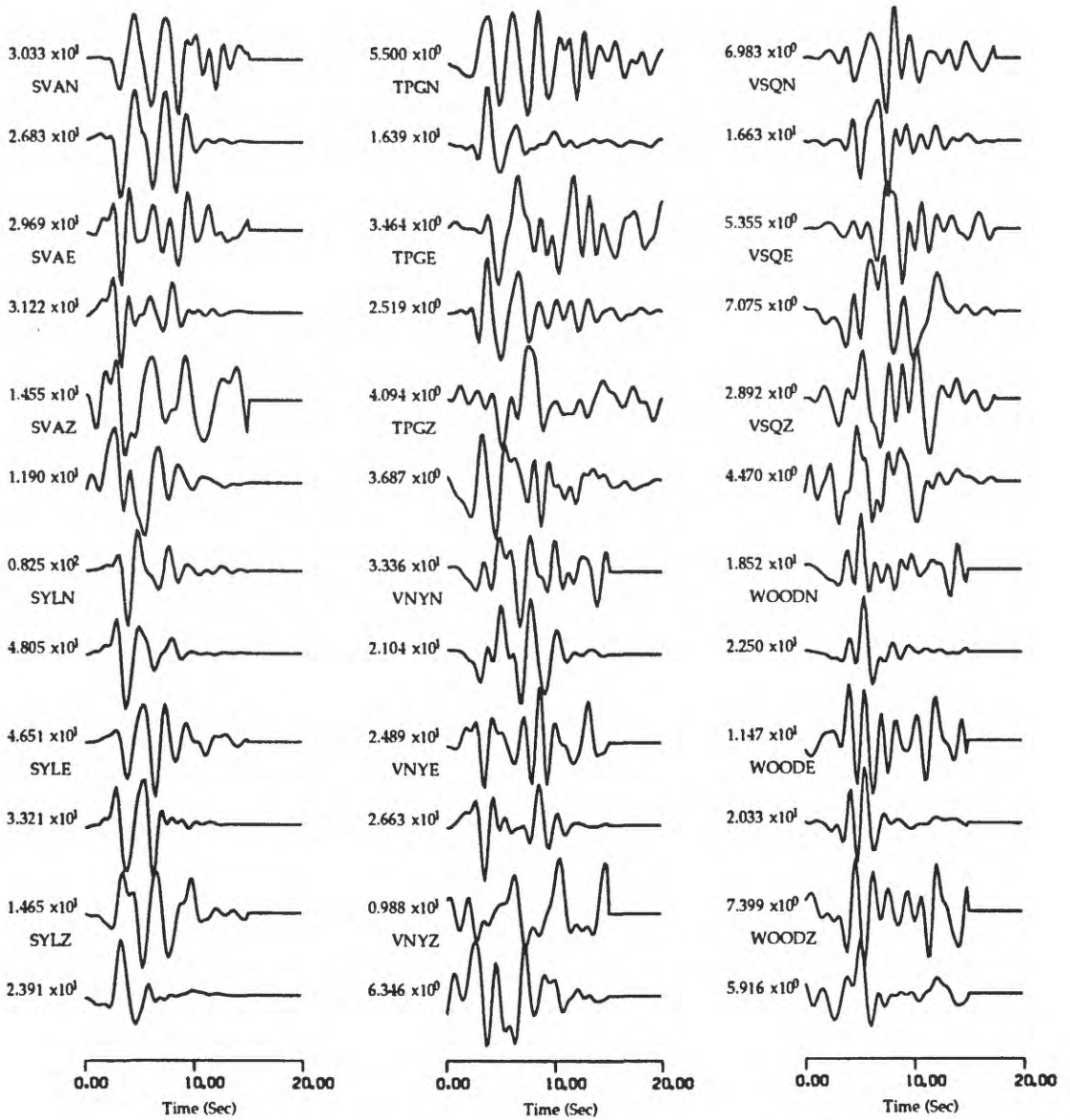
3.033 x10^1
SVAN
2.683 x10^1
2.969 x10^1
SVAE
3.122 x10^1
1.455 x10^1
SVAZ
1.190 x10^1
0.825 x10^2
SYLN
4.805 x10^1
4.651 x10^1
SYLE
3.321 x10^1
1.465 x10^1
SYLZ
2.391 x10^1
0.00
10.00
20.00
Time (Sec)
5.500 x10^0
TPGN
1.639 x10^1
3.464 x10^0
TPGE
2.519 x10^0
4.094 x10^0
TPGZ
3.687 x10^0
3.336 x10^1
VNYN
2.104 x10^1
2.489 x10^1
VNYE
2.663 x10^1
0.988 x10^1
VNYZ
6.346 x10^0
0.00
10.00
20.00
Time (Sec)
6.983 x10^0
VSQN
1.663 x10^1
5.355 x10^0
VSQE
7.075 x10^0
2.892 x10^0
VSQZ
4.470 x10^0
1.852 x10^1
WOODN
2.250 x10^1
1.147 x10^1
WOODE
2.033 x10^1
7.399 x10^0
WOODZ
5.916 x10^0
0.00
10.00
20.00
Time (Sec)

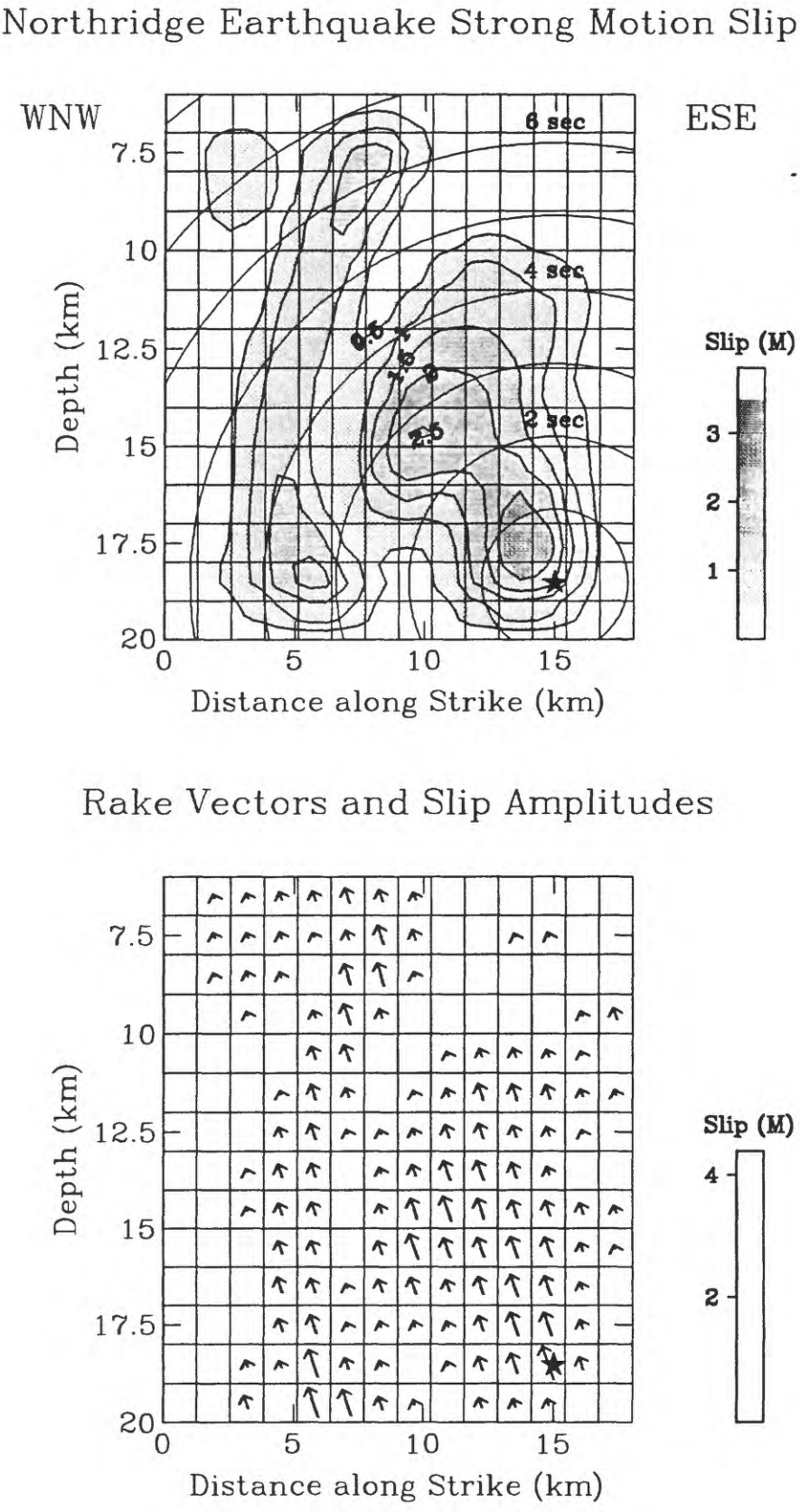
Northridge Earthquake Strong Motion Slip
WNW
ESE
6 sec
4 sec
2 sec
0.5
1.5
2.5
Slip (M)
3
2
1
Depth (km)
7.5
10
12.5
15
17.5
20
0
5
10
15
Distance along Strike (km)
Rake Vectors and Slip Amplitudes
Slip (M)
4
2
Depth (km)
7.5
10
12.5
15
17.5
20
0
5
10
15
Distance along Strike (km)

Figure 7

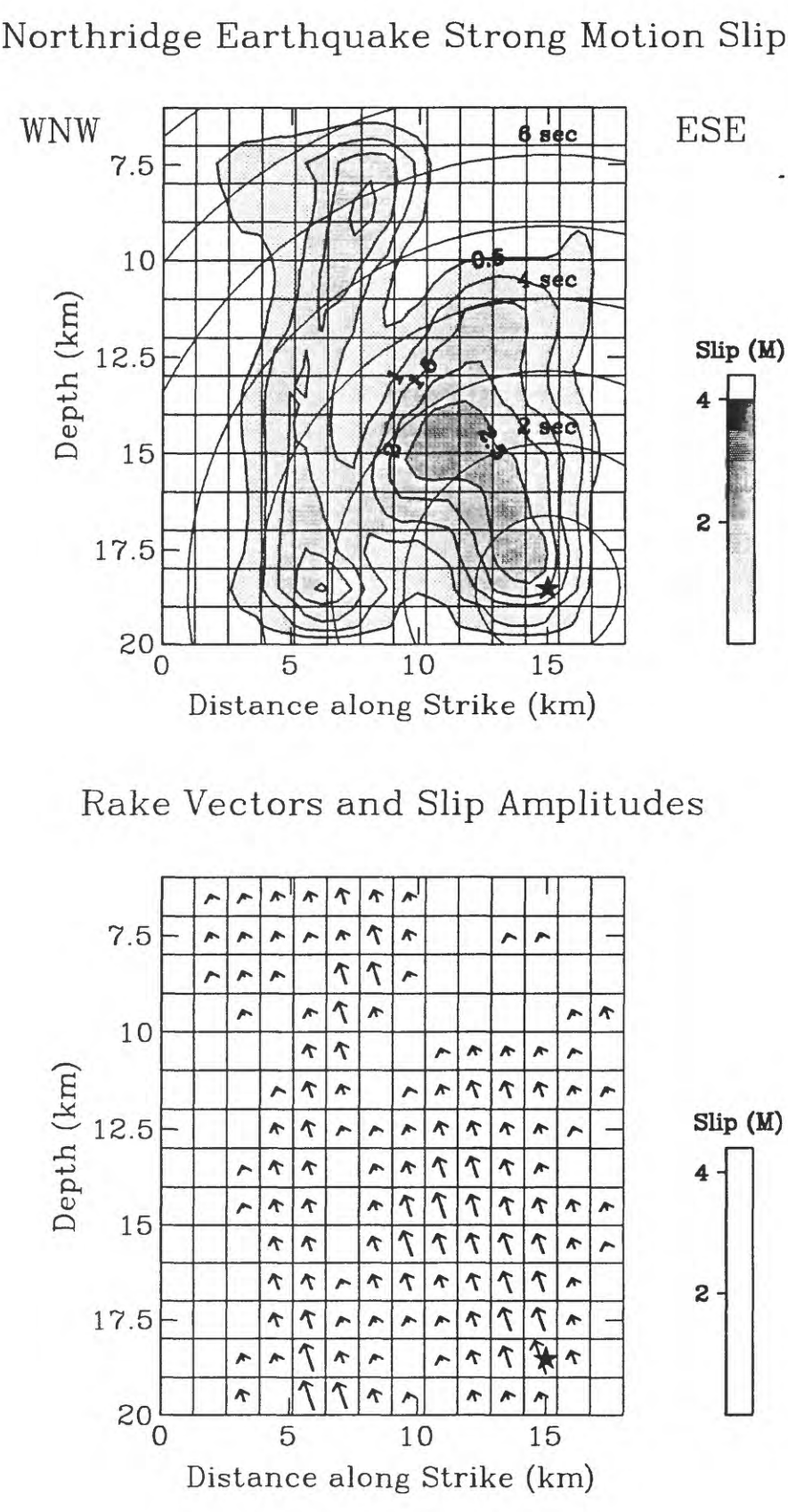
Northridge Earthquake Strong Motion Slip
WNW
ESE
6 sec
4 sec
2 sec
0.5
Slip (M)
4
2
Depth (km)
7.5
10
12.5
15
17.5
20
0
5
10
15
Distance along Strike (km)
Rake Vectors and Slip Amplitudes
Slip (M)
4
2
Depth (km)
7.5
10
12.5
15
17.5
20
0
5
10
15
Distance along Strike (km)

Figure 8

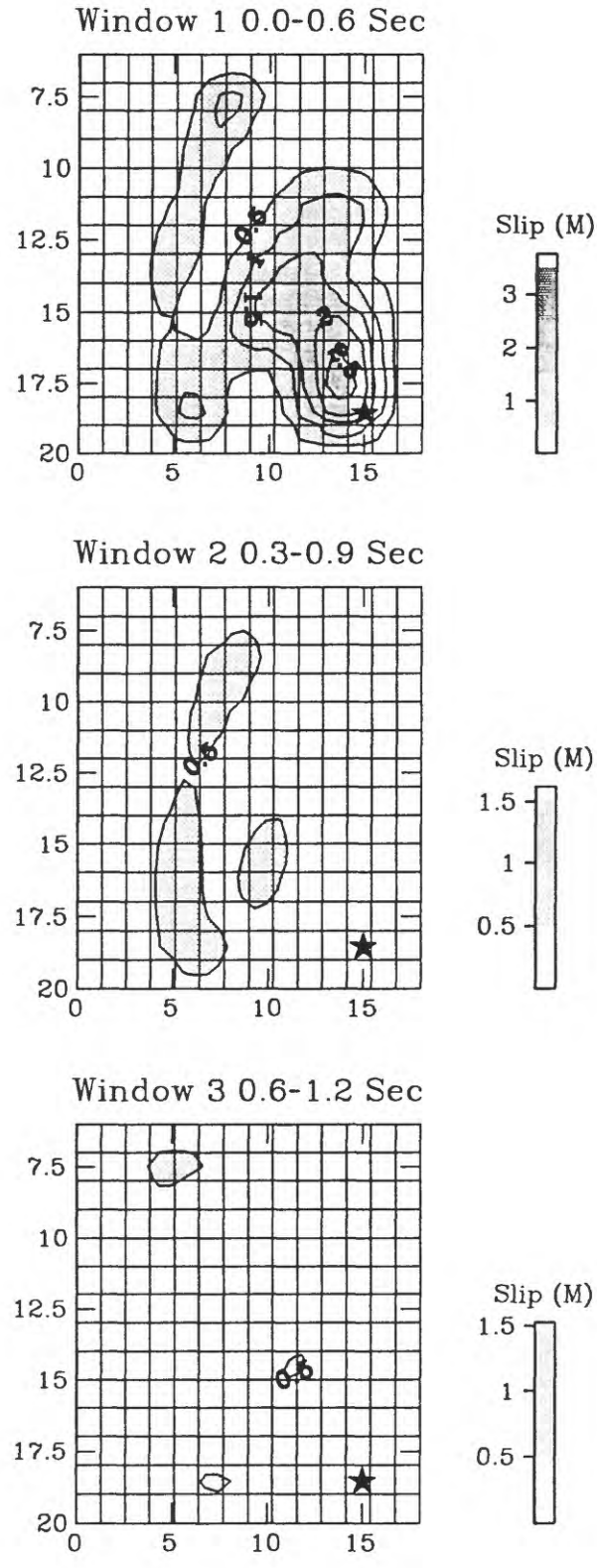
Window 1 0.0-0.6 Sec
7.5
10
12.5
15
17.5
20
0
5
10
15
Slip (M)
3
2
1
Window 2 0.3-0.9 Sec
7.5
10
12.5
15
17.5
20
0
5
10
15
Slip (M)
1.5
1
0.5
Window 3 0.6-1.2 Sec
7.5
10
12.5
15
17.5
20
0
5
10
15
Slip (M)
1.5
1
0.5

Figure 9

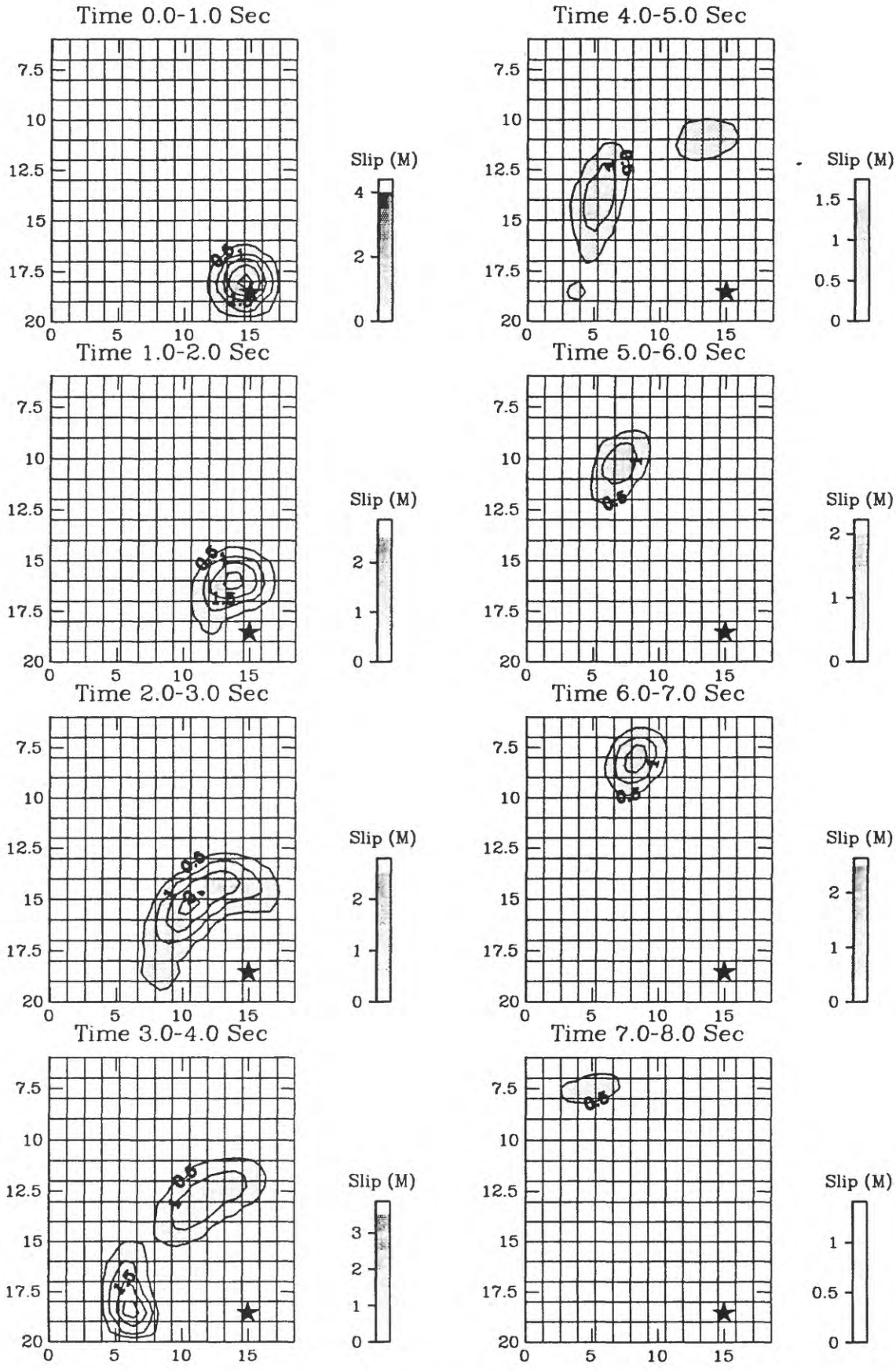
Time 0.0-1.0 Sec
Time 1.0-2.0 Sec
Time 2.0-3.0 Sec
Time 3.0-4.0 Sec
Time 4.0-5.0 Sec
Time 5.0-6.0 Sec
Time 6.0-7.0 Sec
Time 7.0-8.0 Sec
Slip (M)
7.5
10
12.5
15
17.5
20
0
5
10
15

Figure 10

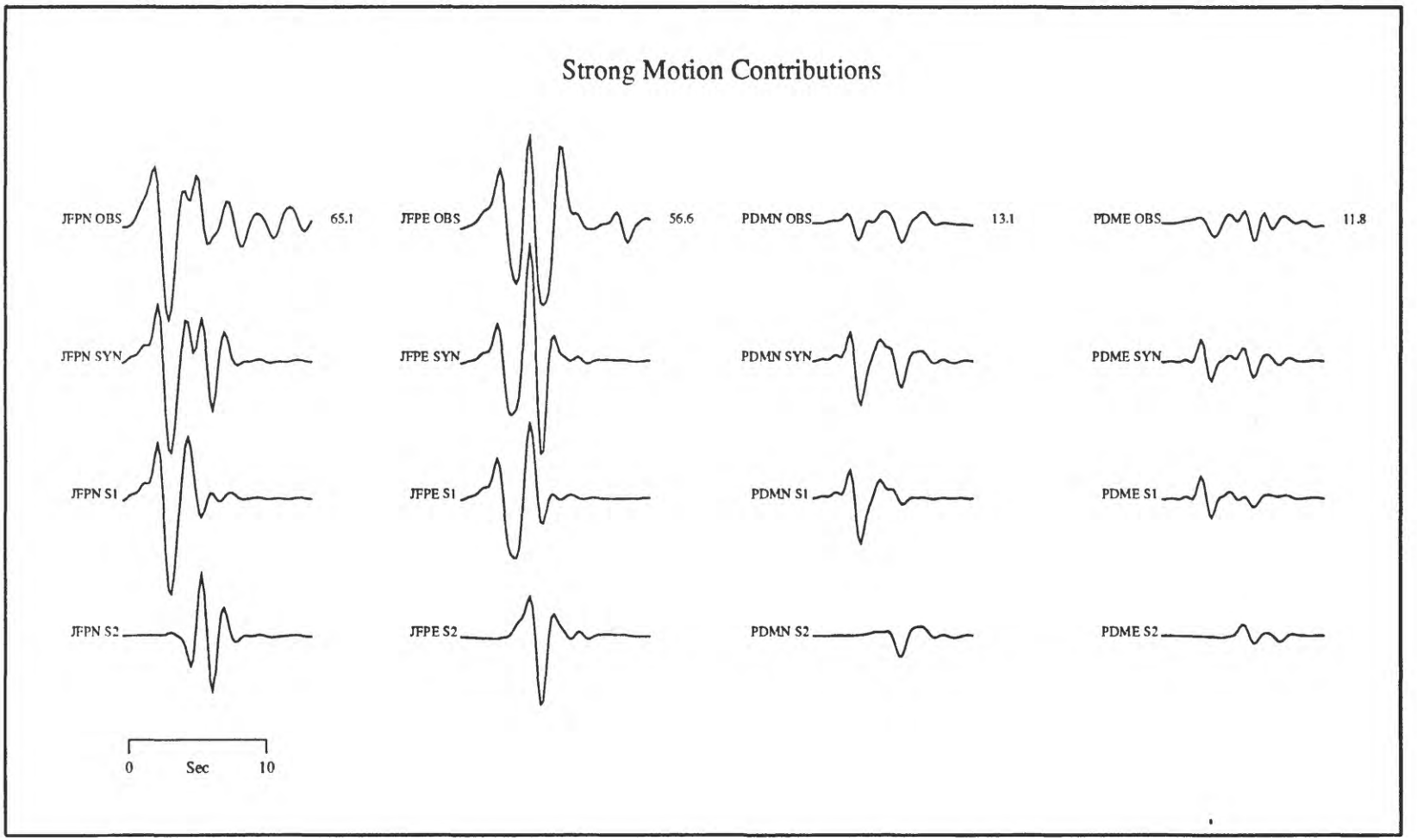
Strong Motion Contributions
JFPN OBS
65.1
JFPE OBS
56.6
PDMN OBS
13.1
PDME OBS
11.8
JFPN SYN
JFPE SYN
PDMN SYN
PDME SYN
JFPN S1
JFPE S1
PDMN S1
PDME S1
JFPN S2
JFPE S2
PDMN S2
PDME S2
0
Sec
10

Figure 11a

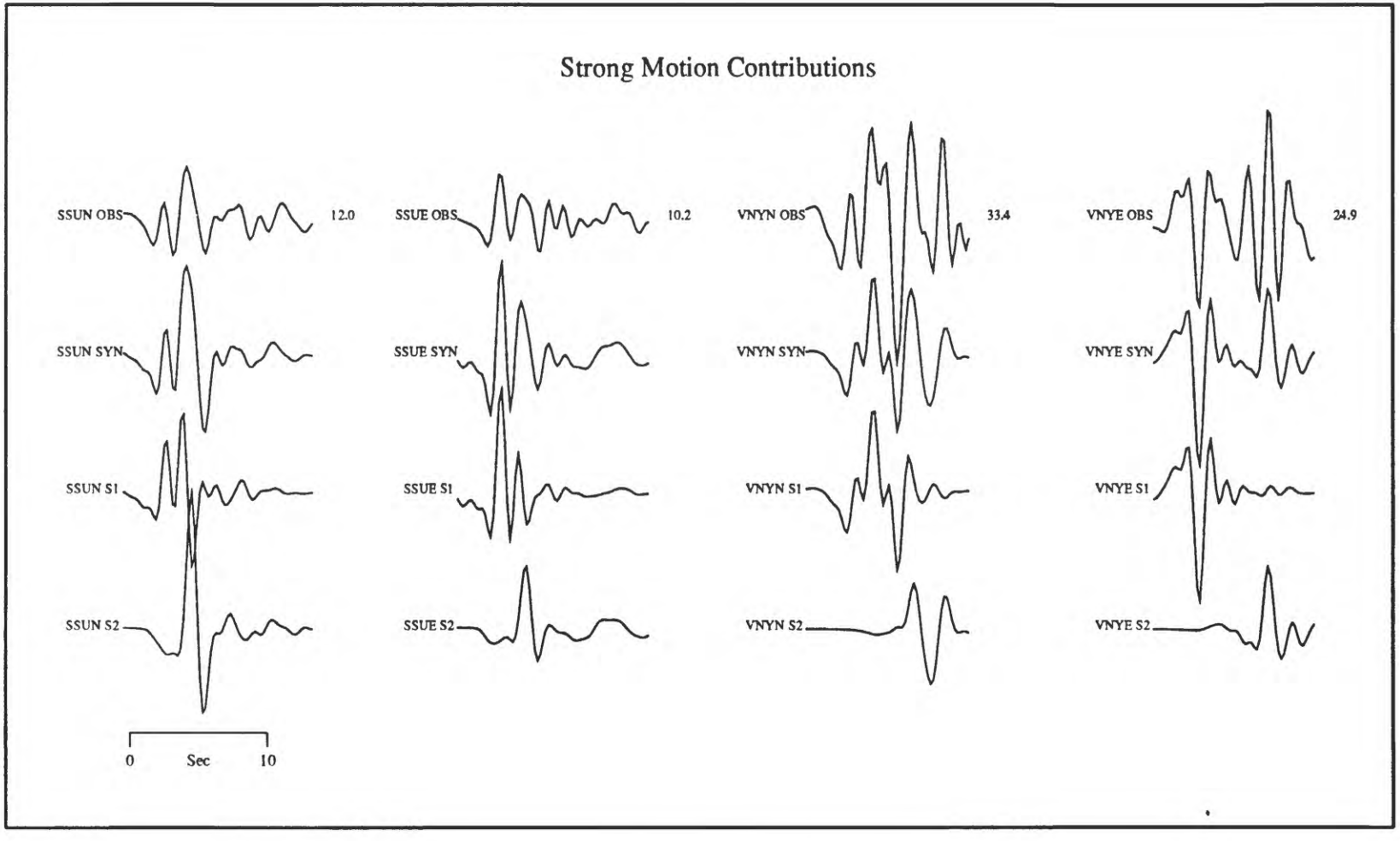
Strong Motion Contributions
SSUN OBS
12.0
SSUN SYN
SSUN S1
SSUN S2
SSUE OBS
10.2
SSUE SYN
SSUE S1
SSUE S2
VNYN OBS
33.4
VNYN SYN
VNYN S1
VNYN S2
VNYE OBS
24.9
VNYE SYN
VNYE S1
VNYE S2
0
Sec
10

Figure 11b

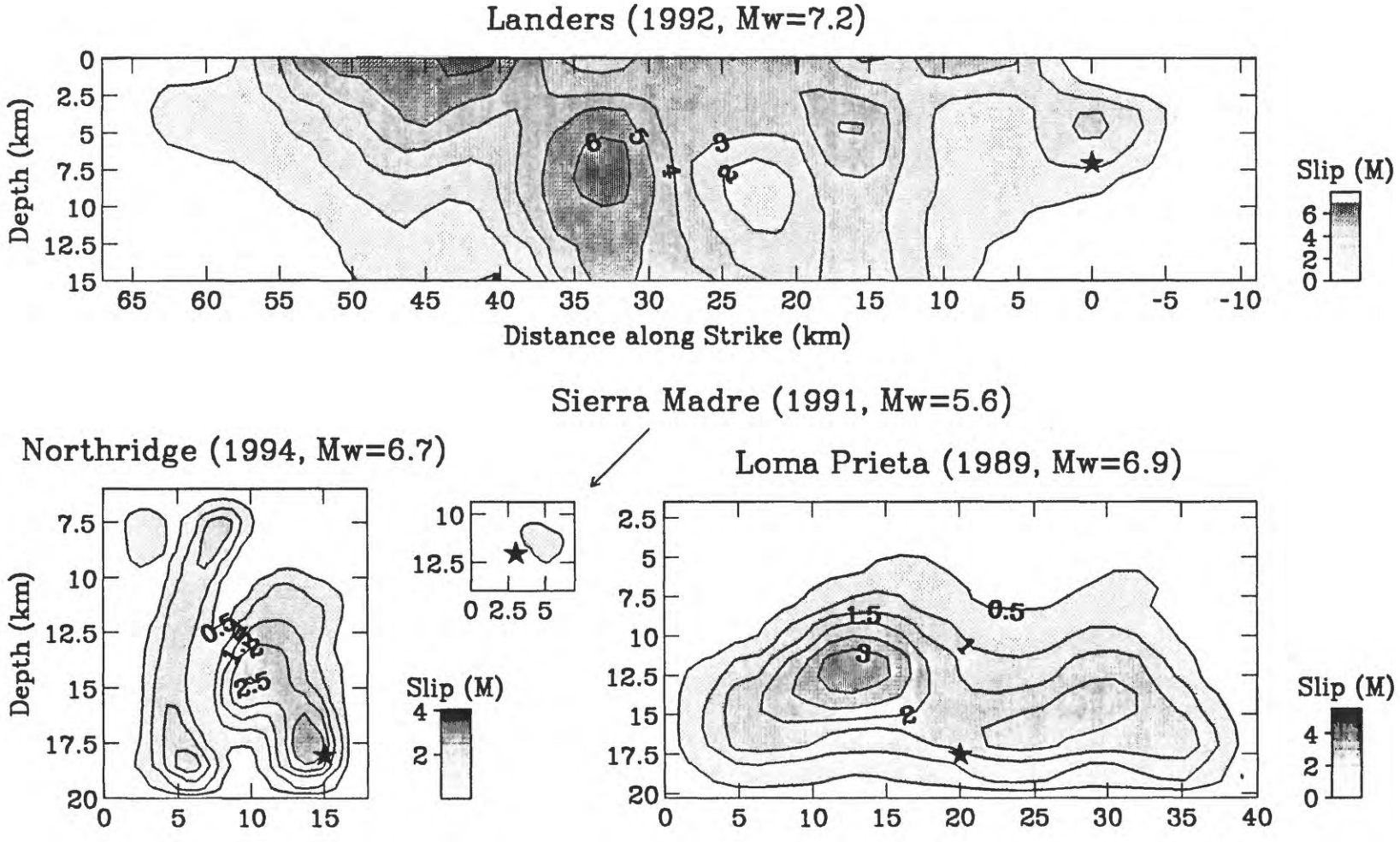

Figure 12

— PAGE 48 FOLLOWS —

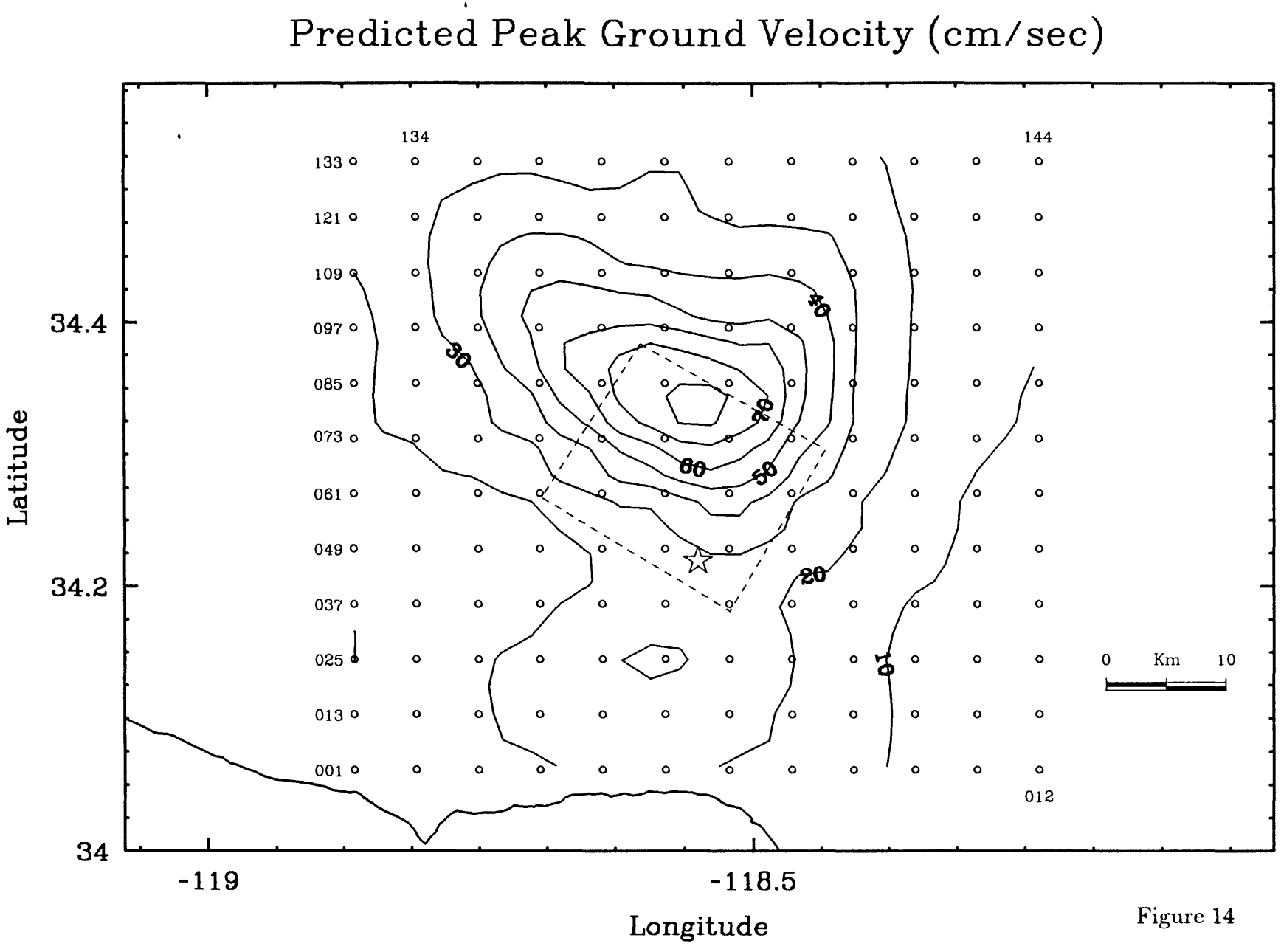
Predicted Peak Ground Velocity (cm/sec)
134
144
133
121
109
097
085
073
061
049
037
025
013
001
012
34.4
34.2
34
Latitude
-119
-118.5
Longitude
30
40
60
50
20
10
0 Km 10

Figure 14

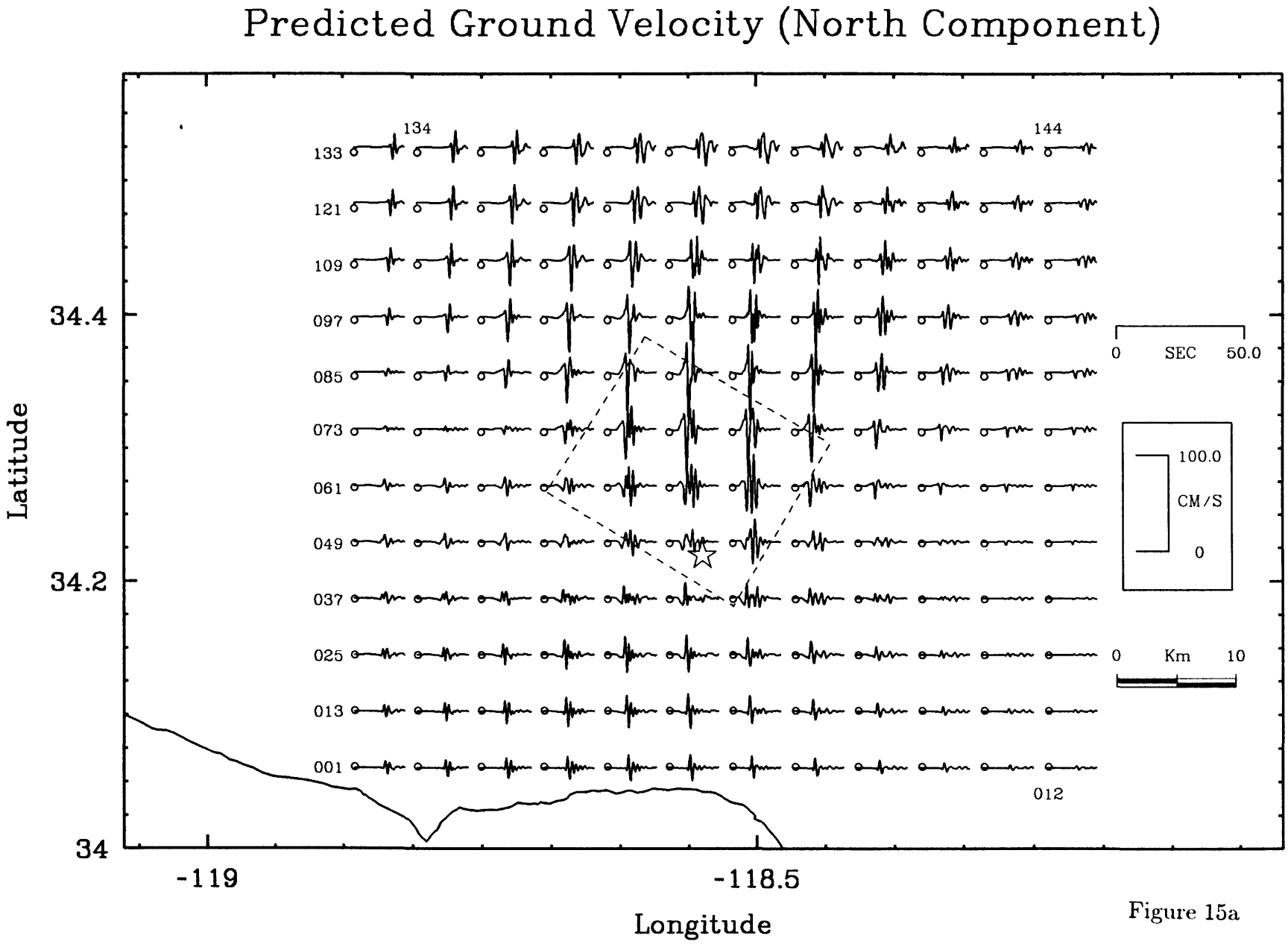
Predicted Ground Velocity (North Component)
134
144
133
121
109
097
085
073
061
049
037
025
013
001
012
34.4
34.2
34
Latitude
-119
-118.5
Longitude
0 SEC 50.0
100.0
CM/S
0
0 Km 10

Figure 15a

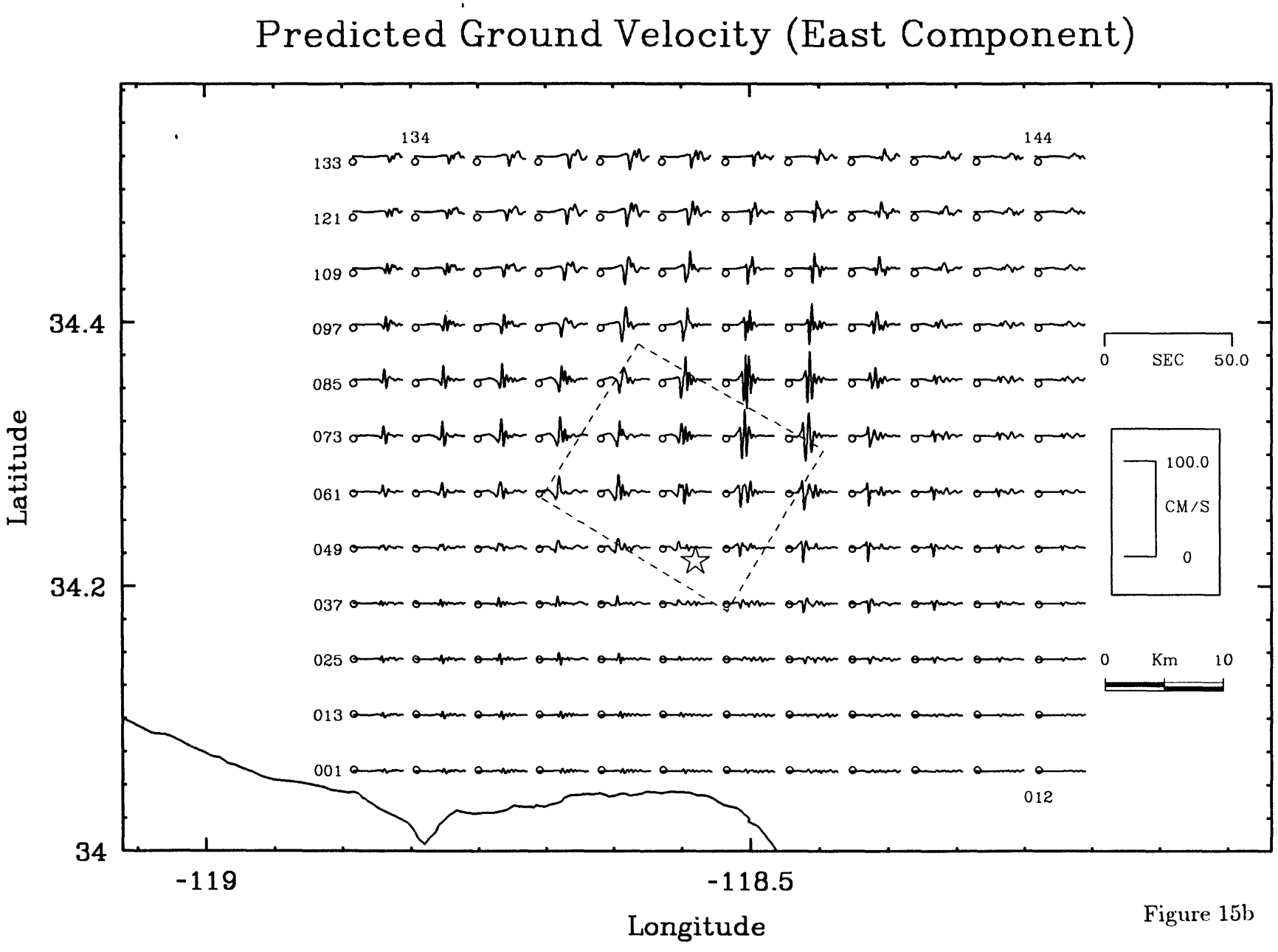
Predicted Ground Velocity (East Component)
134
144
133
121
109
097
085
073
061
049
037
025
013
001
012
34.4
34.2
34
0 SEC 50.0
100.0
CM/S
0
0 Km 10
Latitude
-119
-118.5
Longitude

Figure 15b

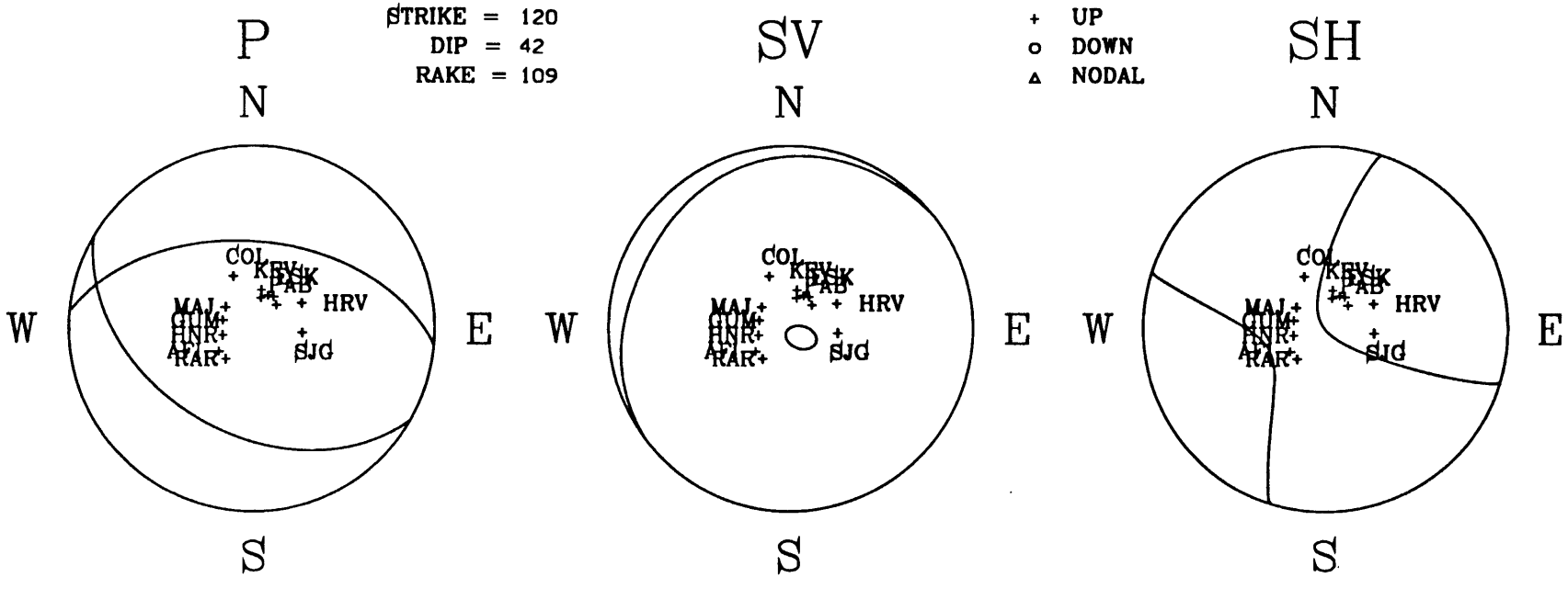
Jan 17, 1994 Northridge
STRIKE = 120
DIP = 42
RAKE = 109
+ UP
o DOWN
△ NODAL
P
SV
SH
N
W
E
S
COL
KBV
PAB
HRV
SJG
MAJ
CUM
HNR
RAR

Figure 16

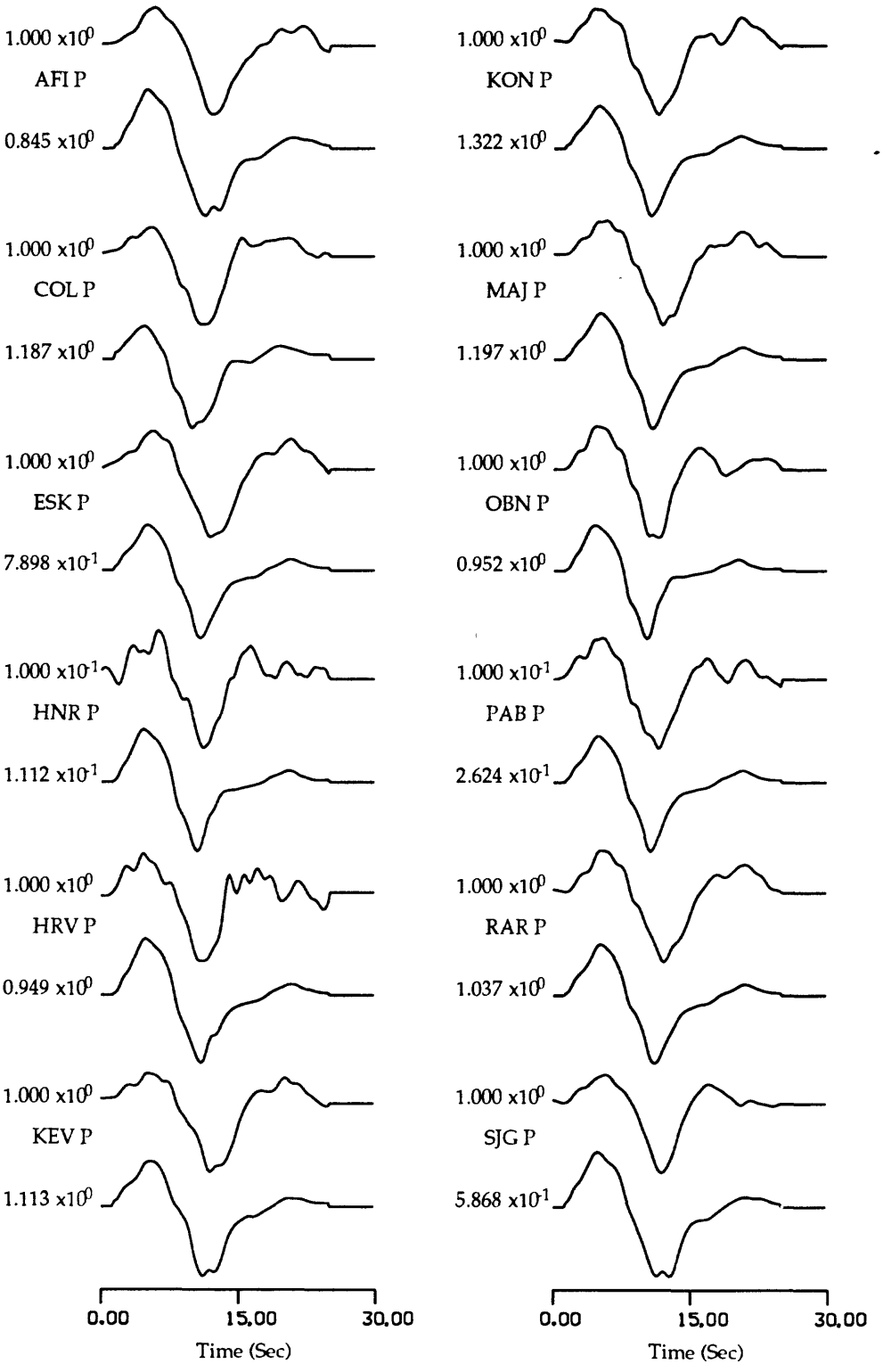
TELESEISMIC P WAVES (DISPLACEMENT)
1.000 x10^0
AFI P
0.845 x10^0
1.000 x10^0
COL P
1.187 x10^0
1.000 x10^0
ESK P
7.898 x10^-1
1.000 x10^-1
HNR P
1.112 x10^-1
1.000 x10^0
HRV P
0.949 x10^0
1.000 x10^0
KEV P
1.113 x10^0
1.000 x10^0
KON P
1.322 x10^0
1.000 x10^0
MAJ P
1.197 x10^0
1.000 x10^0
OBN P
0.952 x10^0
1.000 x10^-1
PAB P
2.624 x10^-1
1.000 x10^0
RAR P
1.037 x10^0
1.000 x10^0
SJG P
5.868 x10^-1
0.00
15.00
30.00
Time (Sec)
0.00
15.00
30.00
Time (Sec)

Figure 17a

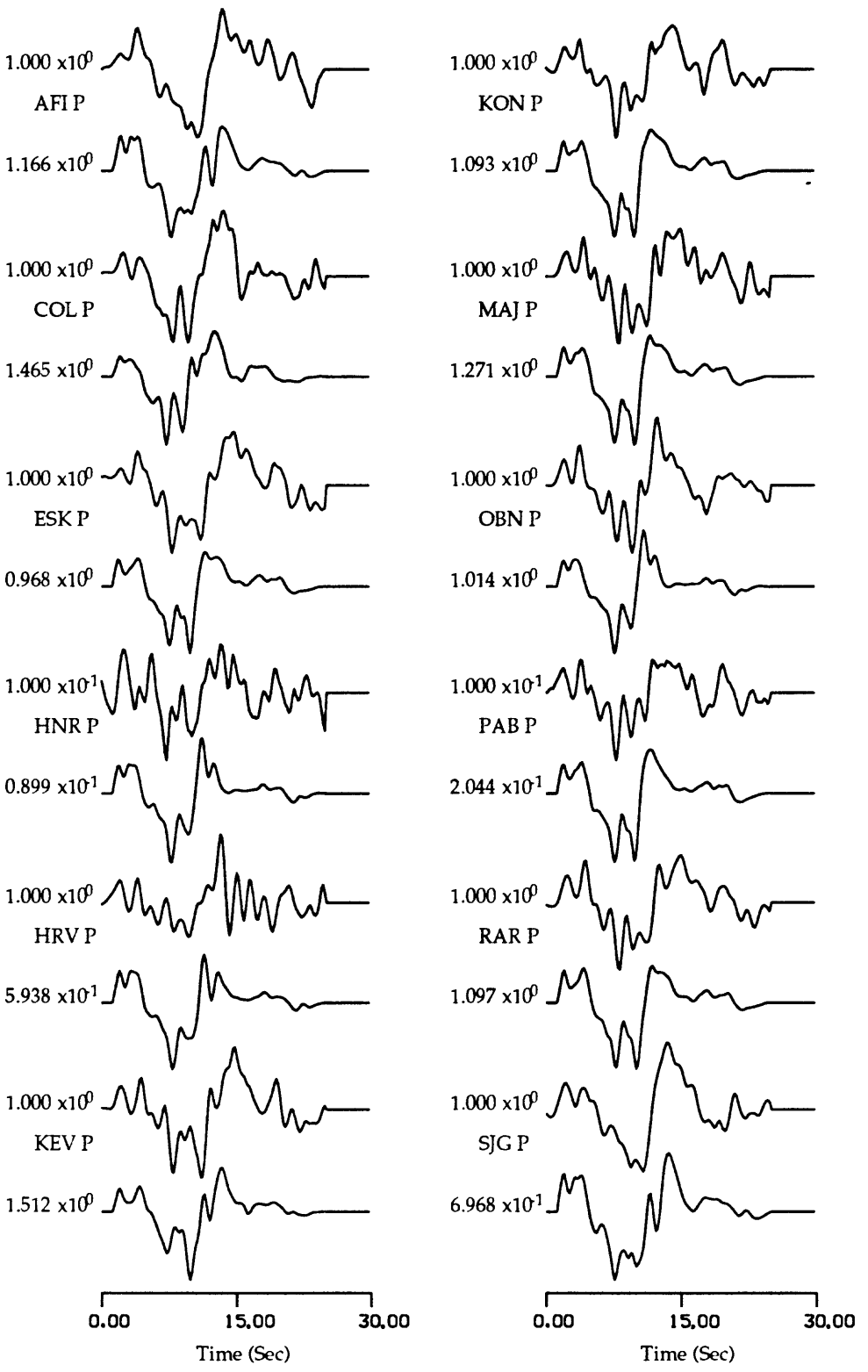
TELESEISMIC P WAVES (VELOCITY)
1.000 x10^0
AFI P
1.166 x10^0
1.000 x10^0
COL P
1.465 x10^0
1.000 x10^0
ESK P
0.968 x10^0
1.000 x10^-1
HNR P
0.899 x10^-1
1.000 x10^0
HRV P
5.938 x10^-1
1.000 x10^0
KEV P
1.512 x10^0
1.000 x10^0
KON P
1.093 x10^0
1.000 x10^0
MAJ P
1.271 x10^0
1.000 x10^0
OBN P
1.014 x10^0
1.000 x10^-1
PAB P
2.044 x10^-1
1.000 x10^0
RAR P
1.097 x10^0
1.000 x10^0
SJG P
6.968 x10^-1
0.00
15.00
30.00
Time (Sec)
0.00
15.00
30.00
Time (Sec)

Figure 17b